

Submitted to the ApJ

Special Relativistic Simulations of Magnetically-dominated Jets in Collapsing Massive Stars

Tomoya Takiwaki¹, Kei Kotake^{2,3}, and Katsuhiko Sato^{1,4,5}

¹*Department of Physics, School of Science, the University of Tokyo, 7-3-1 Hongo, Bunkyo-ku, Tokyo 113-0033, Japan*

takiwaki@utap.phys.s.u-tokyo.ac.jp

²*Division of Theoretical Astronomy, National Astronomical Observatory of Japan, 2-21-1, Osawa, Mitaka, Tokyo, 181-8588, Japan*

³*Max-Planck-Institut für Astrophysik, Karl-Schwarzschild -Str. 1, D-85741, Garching, Germany*

kkotake@th.nao.ac.jp, kotake@MPA-Garching.MPG.DE

⁴*Research Center for the Early Universe, School of Science, the University of Tokyo, 7-3-1 Hongo, Bunkyo-ku, Tokyo 113-0033, Japan*

⁵*The Institute for the Physics and Mathematics of the Universe, The University of Tokyo, Kashiwa, Chiba, 277-8568 Japan*

ABSTRACT

We perform a series of two-dimensional magnetohydrodynamic core-collapse simulations of rapidly rotating and strongly magnetized massive stars. To study the properties of magnetic explosions for a longer time stretch of postbounce evolution, we develop a new code under the framework of special relativity including a realistic equation of state with a multiflavor neutrino leakage scheme. Our results show the generation of the magnetically-dominated jets in the two ways. One is launched just after the core-bounce in a prompt way and another is launched at ~ 100 ms after the stall of the prompt shock. We find that the shock-revival occurs when the magnetic pressure becomes strong, due to the field wrapping, enough to overwhelm the ram pressure of the accreting matter. The critical toroidal magnetic fields for the magnetic shock-revival are found to be

universal of $\sim 10^{15}\text{G}$ behind the jets. We point out that the time difference before the shock-revival has a strong correlation with the explosions energies. Our results suggest that the magnetically dominated jets are accompanied by the formation of the magnetars. Since the jets are mildly relativistic, we speculate that they might be the origin of some observed X-ray flashes.

Subject headings: supernovae: collapse, rotation — magnetars: pulsars, magnetic field — methods: numerical — MHD — special relativity — gamma rays: bursts

1. Introduction

2. Introduction

There have been growing evidences shedding lights on the relations between the high energy astrophysical phenomena and their origins. A number of host galaxies of long-duration gamma-ray bursts (GRBs) are recently identified as metal poor galaxies whose metallicities are lower than that of average massive star-forming galaxies (Savaglio et al. 2006; Stanek et al. 2006, and reference therein). The preponderance of short-lived massive star formation in such young galaxies, as well as the identification of SN Ib/c light curves peaking after the bursts in a few cases, has provided strong support for a massive stellar collapse origin of the long GRBs (Paczynski 1998; Galama et al. 1998; Stanek et al. 2003). The duration of the long GRBs may correspond to the accretion of debris falling into the central black hole (BH) (Piro et al. 1998), which suggests the observational consequence of the BH formation likewise the supernova or neutron star formation. There is also a growing observational evidence of supermagnetized neutron stars with the magnetic fields of $\sim 10^{14} - 10^{15}\text{G}$, the so-called magnetars (Duncan & Thompson (1992), see Lattimer & Prakash (2007) for a recent review). The magnetic fields are determined by the measured period and derivative of period under the assumption that the spin-down is caused due to the usual magnetic dipole radiation (Zhang & Harding 2000; Harding & Lai 2006). Tentative detections of spectral features during the burst phase also indicate $B \sim 10^{15}\text{G}$ when interpreted as proton cyclotron lines (Gavril et al. 2002; Ibrahim et al. 2003; Rea et al. 2003). Recently X-ray flash (XRF), which is a low energy analogue of the GRB, is receiving great attentions as a possible relevance to the magnetar formations (Mazzali et al. 2006; Toma et al. 2007). A large amount of neutron rich Ni ejected by SN2006aj associated with XRF060218 is interpreted to be the formation of such objects, not the black hole after the explosion (Maeda et al. 2007a).

So far a number of numerical simulations have been done towards the understanding of the formation mechanisms of these compact objects such as neutron stars, magnetars, and

the black holes in combination with their possible consequences like GRBs and XRFs. The leading model for the long-duration GRBs is the collapsar model (MacFadyen & Woosley 1999). In the model, the core of massive stars with significant angular momentum collapses into a black hole (BH). The neutrinos emitted from the rotation-supported accretion disk around the BH heat the matter of the funnel region of the disk, to launch the GRB outflows. The relativistic flows are expected to ultimately form a fireball, which is good for the explanation of the observed afterglow (e.g., Piran (1999)). In addition, it is suggested that the strong magnetic fields in the cores of order of 10^{15}G play also an active role both for driving the magnetically-driven jets and for extracting a significant amount of energy from the central engine (e.g., Usov (1992); Wheeler et al. (2000); Thompson et al. (2004); Uzdensky & MacFadyen (2007a) and see references therein).

In order to understand such scenarios, the ultimate necessity of the stellar core-collapse simulations is to perform the simulations tracing all the phases in a consistent manner starting from the stellar core-collapse, core-bounce, shock-stall, stellar explosion (phase 1) or BH formation and the formation of accretion disk (phase 2), energy deposition to the funnel region by neutrinos and/or magnetic fields (phase 3), to the launching of the fireballs (phase 4). Here for convenience we call each stage as phase 1,2, etc. The requirement for the numerical modeling to this end is highly computationally expensive, namely the multidimensional MHD simulations not only with general relativity for handling the BH formation, but also with the multi-angle neutrino transfer for treating highly anisotropic neutrino radiation from the disks. So various approximative approaches to each phase have been undertaken. As we mention below, these studies are complimentary in the sense that the different epochs are focused on, with the different initial conditions for the numerical modeling being taken.

In addition to the elaborate studies in the conventional supernova context (see recent reviews for Kotake et al. (2006); Janka et al. (2007)), much attention has been paid recently to the roles of rapid rotation and magnetic fields for studying the formation of magnetars and its possible application to the collapsars (Yamada & Sawai 2004; Takiwaki et al. 2004; Kotake et al. 2004b; Sawai et al. 2005; Matt et al. 2006; Moiseenko et al. 2006; Obergaulinger et al. 2006; Nishimura et al. 2006; Burrows et al. 2007; Cerdá-Durán et al. 2007; Scheidegger et al. 2007). After the failed or weak explosion, the accretion to the central objects may lead to the formation of a BH (phase 2). Several general relativistic studies are on the line for the understanding of the hydrodynamics at the epoch of the BH formation, in which more massive progenitors ($>\sim 25M_{\odot}$) than those of the study in the phase 1 are generally employed (Shibata et al. 2006; Sekiguchi & Shibata 2007). Treating the BH as an absorbing boundary or using the fixed metric approaches, the numerical studies of the phase 3 are concerned with the initiation of the outflows from the funnel region of the disk to the acceleration of the jets

as a result of the neutrino heating and/or MHD processes till the jets become mildly relativistic (Koide et al. 1998; MacFadyen & Woosley 1999; Proga et al. 2003; Nishikawa et al. 2005; De Villiers et al. 2005; Krolik et al. 2005; Hawley & Krolik 2006; Mizuno et al. 2006; Fujimoto et al. 2006; McKinney & Narayan 2007; Komissarov & McKinney 2007; Nagataki et al. 2007; Suwa et al. 2007b,a). Numerical studies of the phase 4 are mainly concerned with the dynamics later on, namely, the jet propagation to the breakout from the star, when the acceleration of the jets to the high Lorentz factor is expected (Stone & Hardee 2000; Aloy et al. 2000; Zhang et al. 2003; Leismann et al. 2005; Mizuta et al. 2006; Mizuno et al. 2007).

Our previous study was devoted to the phase 1, in which we performed a series of 2D core-collapse simulations of rotating and magnetized massive stars under the framework of the Newtonian magnetohydrodynamics (Takiwaki et al. 2004). We found that the magneto-driven jet-like shocks were launched from the protoneutron stars just after core-bounce. However at the moment, we were unable to follow the dynamics much later on until when the collimated jets reach further out from the center. The Alfvén velocity of the jet propagating into the outer layer of the iron core can be estimated by the following simple order-of-magnitude estimation,

$$v_A = \frac{B}{\sqrt{4\pi\rho}} \sim 10^{10} \text{cm/s} \frac{B/10^{13}\text{G}}{\sqrt{\rho/(10^5\text{g/cm}^3)}}, \quad (1)$$

with ρ and B being the typical density and magnetic field there. It can be readily inferred that the Alfvén velocity can exceed the speed of light unphysically in the Newtonian simulation. To avoid this problem we construct a new code under the framework of special relativistic magnetohydrodynamics. We take a wider parametric range for the strength of the rotation than that of our previous work. By so doing, we hope to study more systematically than before how the strong magnetic fields and the rapid rotation affect the properties of the magnetic explosions.

We summarize the numerical methods in section 3. Section 3 is devoted to the initial models. In section 4, we show the numerical results. In section 5, we summarize our study and discuss the implications of our model for the magnetars and the X-ray flashes. Details of the numerical scheme and the code tests are given in the appendix.

3. Numerical Methods

The results presented in this paper are calculated by the newly developed special relativistic magnetohydrodynamic (SRMHD) code. The novel point of this code is that the detailed microphysical processes relevant for the stellar-core-collapse simulations are also

coupled to the magneto-hydrodynamics (MHD). We briefly summarize the numerical methods in the following.

The MHD part of the code is based on the formalism of De Villiers et al. (2003). Before going to the basic equations, we write down the definition of the primary code variables. The state of the relativistic fluid element at each point in the space time is described by its density, ρ ; specific energy, e ; velocity, v^i ; and pressure, p . And the magnetic field in the rest frame of the fluid is described by the 4-vector $\sqrt{4\pi}b^\mu = {}^*F^{\mu\nu}U_\nu$, where ${}^*F^{\mu\nu}$ is the dual of the electro-magnetic field strength tensor and U_ν is the 4-velocity.

After some mathematical procedures presented in Appendix A, the basic equations of SRMHD are described as follows:

$$\frac{\partial D}{\partial t} + \frac{1}{\sqrt{\gamma}} \partial_i \sqrt{\gamma} D v^i = 0 \quad (2)$$

$$\frac{\partial E}{\partial t} + \frac{1}{\sqrt{\gamma}} \partial_i \sqrt{\gamma} E v^i = -p \frac{\partial W}{\partial t} - \frac{p}{\sqrt{\gamma}} \partial_i \sqrt{\gamma} W v^i - L_\nu \quad (3)$$

$$\begin{aligned} \frac{\partial S_i - b^t b_i}{\partial t} + \frac{1}{\sqrt{\gamma}} \partial_j \sqrt{\gamma} (S_i v^j - b_i b^j) &= -\frac{1}{2} (\rho h (W v_k)^2 - (b_k)^2) \partial_i \gamma^{kk} \\ &\quad - (\rho h W^2 - b^{t^2}) \partial_i \Phi \\ &\quad - \partial_i \left(p + \frac{\|b\|^2}{2} \right) \end{aligned} \quad (4)$$

$$\frac{\partial B^i}{\partial t} + \partial_j (W v^j b^i - W v^i b^j) = 0 \quad (5)$$

$$\partial^k \partial_k \Phi = \rho h W^2 - \left(p + \frac{|b|^2}{2} \right) - (b^t)^2 \quad (6)$$

where $W = \frac{1}{\sqrt{1-v^k v_k}}$, $D = \rho W$, $E = eW$ and $S_i = \rho h W^2 v_i$ are the Lorentz boost factor, auxiliary variables correspond to density, energy, and momentum, respectively. Eq. (2), Eq. (3) and Eq. (4) represents the mass, energy, and momentum conservations. L_ν in the right hand side of Eq. (3) is a total neutrino cooling rate determined by microphysical processes which will be later explained. In Eq. (4) it is noted that the relativistic enthalpy, $h = (1 + e/\rho + p/\rho + |b|^2/\rho)$ includes magnetic energy. Eq. (5) is the induction equation for the magnetic fields. B^i are related to that in the rest frame of fluid as $B^i = W b^i - W b_t b^i$. Here b_t is a time component of the 4-vector, b_μ . Eq. (6) is the Poisson equation for the gravitational potential, Φ .

This newly developed code is an Eulerian code based on the finite-difference method. The numerical approach for solving the basic equations of (2), (3), and (4), consists of the two steps, namely, the transport and the source step. These procedures are essentially the same as

those of ZEUS-2D (Stone & Norman 1992). At the transport step, the second order upwind scheme of Van Leer is implemented (van Leer 1977). To handle the numerical oscillations, we employ an artificial viscosity. In the special relativistic treatments, many forms for the compression heating are possible (Hawley et al. 1984b). In our code, we employ the form of $\frac{\rho h}{\sqrt{\gamma}} \partial_i \sqrt{\gamma} W v^i$ as the compression heating, which becomes the well-known artificial viscosity of von Neumann and Richtmyer under the Newtonian approximation. While not explicitly included in the above expression for the enthalpy, the contribution from the compression heating on the inertia is included in our calculations. The detailed status on the shock capturing using this term are shown at Appendix D.

The time evolution of the magnetic fields are solved by induction equation, Eq. (5). In so doing, the code utilizes the so-called constrained transport method, which ensures the divergence free ($\nabla \cdot \mathbf{B} = 0$) of the numerically evolved magnetic fields at all times. Furthermore, the method of characteristics (MOC) is implemented to propagate accurately all modes of MHD waves. The detailed explanation and the numerical tests are delivered in the appendix B. The self-gravity is managed by solving the Poisson equation, Eq. (6) with the incomplete Cholesky decomposition conjugate gradient method.

Together with these hydrodynamic procedures, the following microphysical processes are implemented in this code. We approximate the neutrino transport by a multiflavor leakage scheme (Epstein & Pethick 1981; Rosswog & Liebendörfer 2003), in which three neutrino flavors: electron neutrino, ν_e ; electron antineutrino, $\bar{\nu}_e$; and the heavy-lepton neutrinos, ν_μ , $\bar{\nu}_\mu$, ν_τ , $\bar{\nu}_\tau$ (collectively referred to as ν_X), are taken into account. The neutrino reactions included are electron capture on proton and free nuclei; positron capture on neutron; photo-, pair, plasma processes (Fuller et al. 1985; Takahashi et al. 1978; Itoh et al. 1989, 1990). We added an transport equation for the lepton fraction $Y_l (= Y_e - Y_{e^+} + Y_{\nu_e} - Y_{\bar{\nu}_e})$,

$$\frac{\partial Y_l}{\partial t} + \frac{1}{\sqrt{\gamma}} \partial_i \sqrt{\gamma} Y_l = -\gamma_l \quad (7)$$

to treat their change due to the relevant charged current reactions, whose reaction rates are collectively represented by γ_l here, with $Y_e, Y_{e^+}, Y_{\nu_e}, Y_{\bar{\nu}_e}$, γ_l being electron, positron, electron neutrino, anti-electron neutrino fraction, respectively (see Epstein & Pethick (1981); Rosswog & Liebendörfer (2003); Kotake et al. (2003) for details of the estimation of γ_l). L_ν in Eq. (3) represents the total neutrino cooling rate which is also estimated by the scheme. As for the equation of state (EOS), we employ a realistic one based on the relativistic mean field theory (Shen et al. 1998). Since the pressure is not represented as the analytic function of density and internal energy like in the case of polytropic EOS, an iterative algorithm are employed to update the fundamental variables (see Appendix C for detail).

In our two dimensional simulations, the spherical coordinate is used with $300(r) \times 60(\theta)$

grid points to cover the computational domain. Axial symmetry and reflection symmetry across the equatorial plane are assumed. The radial grid is nonuniform, extending from 0 to $4.0 \times 10^8 \text{cm}$ with finer grid near the center. The finest grid is set to 10^5cm . The polar grid uniformly covers from $\theta = 0$ to $\theta = \frac{\pi}{2}$.

Finally we summarize the difference on the numerical approach from our previous work (Takiwaki et al. 2004). Most major development is the fully special relativistic treatment on magneto-hydrodynamics. And for the microphysical parts the cooling terms by neutrino contains contributions from not only ν_e but also $\bar{\nu}_e$ and ν_X . These advances provide more reliable results on the magneto-rotational core-collapse.

4. Initial Models

We make precollapse models by taking the profiles of density, internal energy, and electron fraction distribution from a rotating presupernova model of E25 by Heger & Langer (2000). This model has mass of $25M_\odot$ at the zero age main sequence, however loses the hydrogen envelope and becomes a Wolf Rayet star of $5.45 M_\odot$ before core-collapse. Our computational domain involves the whole iron-core of $1.69M_\odot$. It is noted that this model seems to be a good candidate as a progenitor of the GRB since the lack of the line spectra of the ejected envelopes are reconciled with the observations of the supernovae associated with GRBs (e.g., Meszaros (2006)).

Since little is known about the spatial distributions of the rotation and the magnetic fields in the evolved massive stars (see, however, Spruit (2002)), we add the following rotation and magnetic field profiles in a parametric manner to the non-rotating core mentioned above. For the rotation profile, we assume a cylindrical rotation of

$$\Omega(X, Z) = \Omega_0 \frac{X_0^2}{X^2 + X_0^2} \frac{Z_0^4}{Z^4 + Z_0^4}, \quad (8)$$

where Ω is the angular velocity and X and Z denote distance from the rotational axis and the equatorial plane. We adopt values of the parameters, X_0 and Z_0 , as 10^7cm , 10^8cm , respectively. The parameter, X_0 represents the degree of differential rotation. We assume the strong differential rotation as in our previous study (Takiwaki et al. 2004).

As for the initial configuration of the magnetic fields, we assume that the field is nearly uniform and parallel to the rotational axis in the core and dipolar outside. For the purpose, we consider the following effective vector potential,

$$A_r = A_\theta = 0, \quad (9)$$

$$A_\phi = \frac{B_0}{2} \frac{r_0^3}{r^3 + r_0^3} r \sin \theta, \quad (10)$$

where $A_{r,\theta,\phi}$ is the vector potential in the r, θ, ϕ direction, respectively, r is the radius, r_0 is the radius of the core, and B_0 is the model constant. In this study, we adopt the value of r_0 as 2×10^8 cm which is approximately the size of the iron core at a precollapse stage. This vector potential can produce the uniform magnetic fields when r is small compared with r_0 , and the dipole magnetic fields for vice versa. Since the outer boundary is superposed at $r = 4 \times 10^8$ cm, the magnetic fields are almost uniform in the computational domain as the previous work (Takiwaki et al. 2004). It is noted that this is a far better way than the loop current method for constructing the dipole magnetic fields (Symbalisty 1984), because our method produces no divergence of the magnetic fields near the loop current. We set the outflow boundary conditions for the magnetic fields at the outer boundary of the calculated regions.

We compute 9 models changing the total angular momentum and the strength of magnetic fields by varying the value of Ω_0 and B_0 . The model parameters are shown in Table 1. The models are named after this combination, with the first letters, B12, B11, B10, representing strength of the initial magnetic field, the following letter, TW4.0, TW1.0, TW0.25 representing the initial $T/|W|$, respectively. Here $T/|W|$ indicates the ratio of the rotational energy to the absolute value of the gravitational energy. The corresponding values of Ω_0 are 151rad/s, 76rad/s, 38rad/s for TW4.0, TW1.0, TW0.25, respectively. It is noted that the value of $T/|W|$ is 0.15% of the progenitor by Heger & Langer (2000). By exploring to the models with more rapid rotation, we here hope to study the magnetorotational effects on the dynamics systematically.

Table 1: Models and Parameters

		$T/ W (\%)$		
		0.25%	1.0%	4.0%
$B_0(\text{Gauss})$	10^{10}G	B10TW0.25	B10TW1.0	B10TW4.0
	10^{11}G	B11TW0.25	B11TW1.0	B11TW4.0
	10^{12}G	B12TW0.25	B12TW1.0	B12TW4.0

Note. — Model names are labeled by the initial strength of magnetic fields and rotation. $T/|W|$ represents the ratio of the rotational energy to the absolute value of the gravitational energy. The corresponding values of Ω_0 in Eq. (8) are 151rad/s, 76rad/s, 38rad/s for TW4.0, TW1.0, TW0.25, respectively. B_0 represents the strength of the poloidal magnetic fields (see Eq.(10)). The corresponding values of $E_m/|W|$ is 2.5×10^{-8} , 2.5×10^{-6} and 2.5×10^{-4} for 10^{10}G , 10^{11}G and 10^{12}G , respectively with E_m being the magnetic energy.

5. Results

5.1. Hydrodynamics before Core-Bounce

First of all, we briefly mention the dynamics before core bounce, when the gross features are rather similar among the computed models. The characteristic properties are summarized in Table 2.

The story before core-bounce is almost the same as the canonical core-collapse supernovae with rapid rotation (see, e.g., Kotake et al. (2003)). The core begins to collapse due to electron captures and the photodissociation of the iron nuclei, and eventually experiences the bounce at the subnuclear density by the additional support of the centrifugal forces. In fact, the central densities at bounce becomes smaller and the epoch till bounce is delayed as the initial rotation rates become larger (see ρ_{bnc} and t_{bnc} in Table 2).

As the compression proceeds, the rotational energy increases and reaches a few 10^{52} erg at the moment of the bounce (seen from $T/|W|_{\text{bnc}} \times W_{\text{bnc}}$ in Table 2). Given the same initial rotation rates, the values of $T/|W|_{\text{bnc}}$ do not depend on the initial field strength so much. This means that the angular momentum transfer is negligible before bounce, which is also the case of the Newtonian hydrodynamics (Yamada & Sawai 2004). At bounce, the unshocked core becomes more flattened as the initial rotation rate becomes larger (compare panels in Figure 1). From the table, it is also seen that the amplification rates of the magnetic fields (A_{amp}) are mainly determined by the initial rotational rates. One exception is the model B12TW4.0. Due to very rapid rotation with the highest magnetic fields initially imposed, the model bounces predominantly due to the magnetic force. As a result, the core bounce occurs earlier with the lower central density with less gravitational energy of the inner core than the models with the same initial rotation rate (see Table 2). This earlier magnetically-supported bounce leads to the suppression of the amplification rate, which is exceptionally observed for this model.

In this way, the hydrodynamic properties before bounce are mainly governed by the differences of the initial rotation rates. On the other hand, the differences of the magnetic field strength begin to play an important role on the dynamics later on. We will mention them in detail from the next sections.

Table 2: MHD properties till core bounce

Model Names	$T/ W _{\text{bnc}}$	ρ_{bnc} [10^{14}g/cm^3]	$ W_{\text{bnc}} $ [10^{53}erg]	$E_m/ W _{\text{ini}}$	$E_m/ W _{\text{bnc}}$	A_{amp}	t_{bnc} [ms]
B12TW0.25	0.10	2.1	1.1	2.5×10^{-4}	1.0×10^{-3}	100	245
B11TW0.25	0.10	2.1	1.1	2.5×10^{-6}	1.0×10^{-5}	100	245
B10TW0.25	0.10	2.1	1.1	2.5×10^{-8}	1.0×10^{-7}	100	245
B12TW1.0	0.18	1.3	1.1	2.5×10^{-4}	9.0×10^{-3}	720	295
B11TW1.0	0.18	1.3	1.1	2.5×10^{-6}	7.0×10^{-5}	610	295
B10TW1.0	0.18	1.3	1.1	2.5×10^{-8}	7.0×10^{-7}	610	295
B12TW4.0	0.20	0.095	0.68	2.5×10^{-4}	20×10^{-3}	800	477
B11TW4.0	0.19	0.11	0.74	2.5×10^{-6}	29×10^{-5}	4400	484
B10TW4.0	0.19	0.11	0.74	2.5×10^{-8}	31×10^{-7}	4400	484

Note. — Characteristic properties before core bounce. $T/|W|_{\text{bnc}}$ is the rotational energy per gravitational energy at bounce. ρ_{bnc} is the maximum density at bounce. $E_m/|W|_{\text{ini}}$ and $E_m/|W|_{\text{bnc}}$ is the magnetic energy per the gravitational energy initially and at bounce, respectively. A_{amp} represents the amplification rate of magnetic energy until core bounce, which is defined as $A_{\text{amp}} \stackrel{\text{def}}{=} (E_m|_{\text{bnc}})/(E_m|_{\text{ini}})$. t_{bnc} represents the time till bounce.

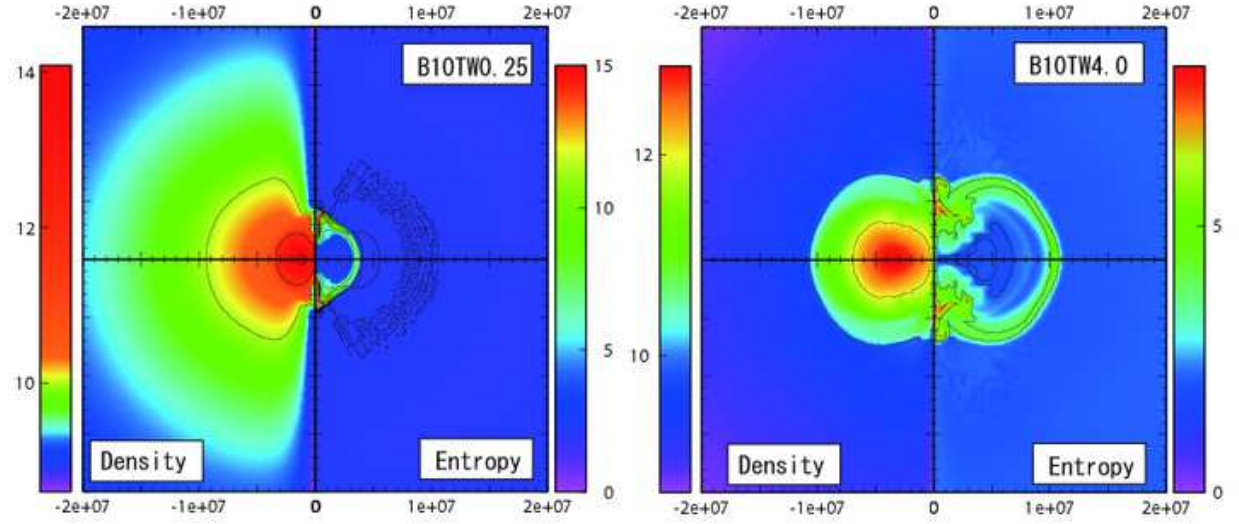


Fig. 1.— Snapshots for models B10TW0.25 (left) and B10TW4.0 (right), showing the degree of the rotational flattening at core bounce. In each panel, contour of density [g/cm^3] (left) and entropy per baryon [k_B] (right) is shown. Flattening of the unshocked core (the central low entropy region seen in the right side of each panel) is remarkable for the right panel. Note that the unit of the horizontal and the vertical axis is in cm.

5.2. Prompt vs. Delayed MHD Exploding Model

After bounce, we can categorize the computed models into two groups, by the criterion whether the shock generated at bounce promptly reach the surface of the iron core or not. For later convenience, we call the former and the latter models as prompt and delayed MHD exploding model, respectively throughout the paper. The models and the corresponding groups are shown in Figure 2. To begin with, we choose typical model from the two groups and mention their properties in detail.

		$T/ W (\%)$		
		0.25%	1.0%	4.0%
$B_0(\text{Gauss})$	10^{10}G	122 ms	96 ms	104 ms
	10^{11}G	72 ms	27 ms	32 ms
	10^{12}G	32 ms	20 ms	25 ms

Fig. 2.— Classification of the computed models into the prompt (red blocks) or delayed (green blocks) MHD exploding model by the difference of $t_{1000\text{km}}$ shown in this table, which is the shock-arrival time to the radius of 1000 km after bounce.

Prompt MHD Exploding Model The models classified into this group have strong magnetic fields and rapid rotation initially. Figure 3 shows the dynamics near core bounce. As seen from the bottom left panel, the shock at core bounce stalls in the direction to the equatorial plane at $\sim 1.4 \times 10^7\text{cm}$ promptly (~ 3 ms) after bounce. However the shock in the direction of the rotational axis does not stall and becomes a collimated jet (see top right and bottom right). The wound-up magnetic fields are an important agent to explain these properties.

The magnetic fields for the promptly MHD models are enough strong to power the jet already at the epoch of bounce. That is clearly shown in the top left panel, showing that the “plasma β ” $\stackrel{\text{def}}{=} p/B^2$, being the ratio of the matter to the matter pressure, outside the unshocked core near the poles becomes very low (typically 10^{-2}). From the right side of the bottom left panel, the toroidal magnetic field strength there reaches over 10^{15}G . The dynamics around the poles are strongly affected by these strong magnetic fields.

The three dimensional plots of Figure 4 are useful to see how the field wrapping occurs. From the top left panel, it is seen that the field lines are strongly wounded around the rotational axis. The white lines in the top right shows the streamlines of the matter. A

fallback of the matter just outside of the head of the jet downwards to the equator (like a cocoon) is seen. In this jet with a cocoon-like structure, the magnetic pressure is always dominant than the matter pressure (see the region where plasma β less than 1 in the right side of the top right panel of Figure 3). This magneto-driven jet does not stall and penetrate to the surface of the iron core. The speed of the head of the jet is mildly relativistic of $\sim 0.3c$, with c being the speed of light (the right side of bottom right panel of Figure 3). At 20 ms after bounce, the jet finally reaches the surface of the iron core of $\sim 10^8$ cm. At this moment, the explosion energy, which will be a useful quantity for comparing the strength of the explosion among the models later, reaches 1.4×10^{50} erg.

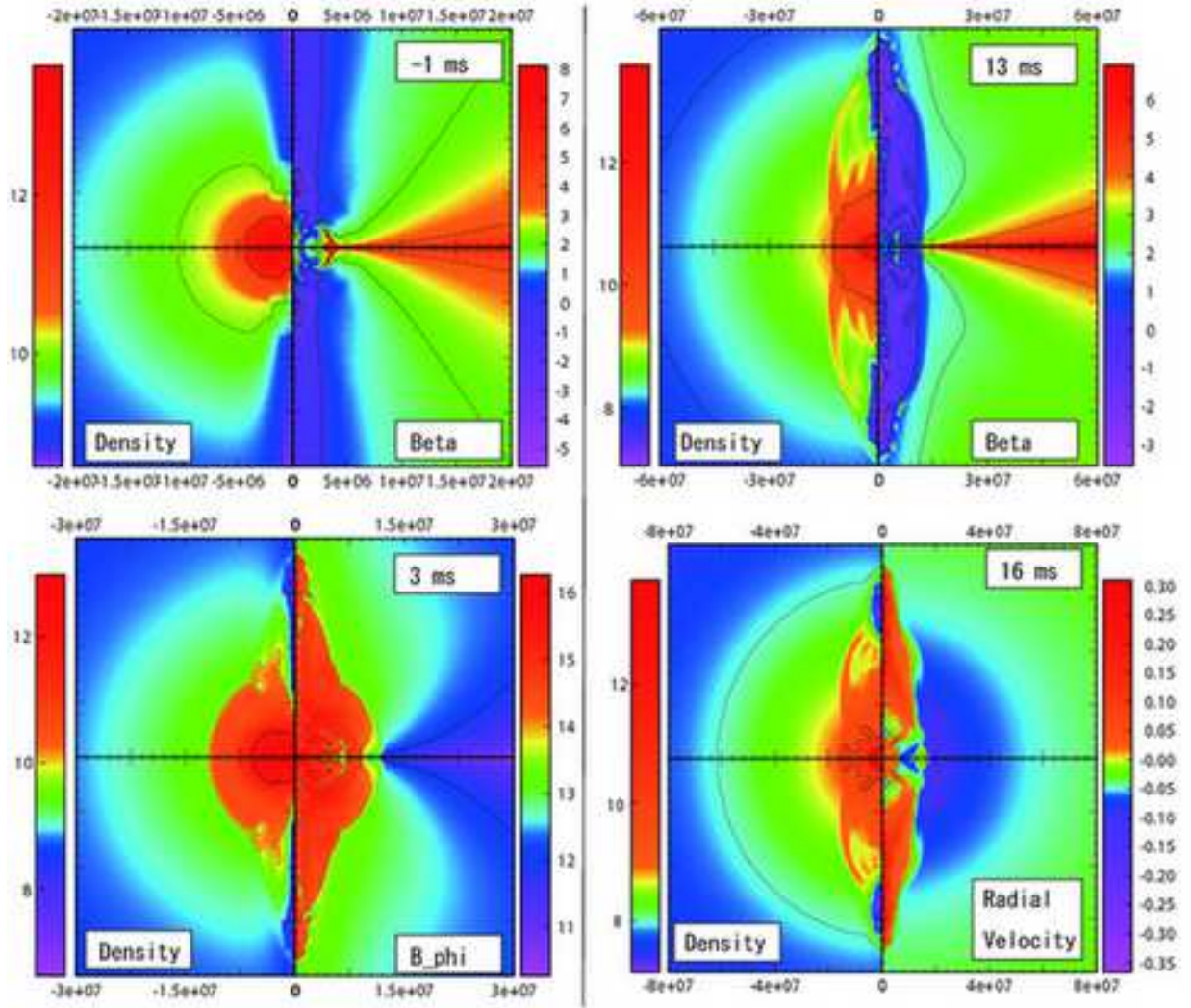


Fig. 3.— Contour of density and various properties after bounce for model B12TW1.0, which belongs to the prompt MHD exploding model. In each panel, the left side represents the logarithm of density [g/cm³]. Time in each panel is measured from the epoch of bounce. At the top panels, the right side is the “plasma β ” $\stackrel{\text{def}}{=} p/\frac{B^2}{8\pi}$, indicated by “Beta”. At the bottom left panel, the right side is the logarithm of toroidal component of the magnetic fields [G], indicated by “ B_{phi} ”. At the bottom right panel, the right side is the radial velocity in unit of the speed of light : c . Note that the unit of the horizontal and the vertical axis of all panels is in [cm].

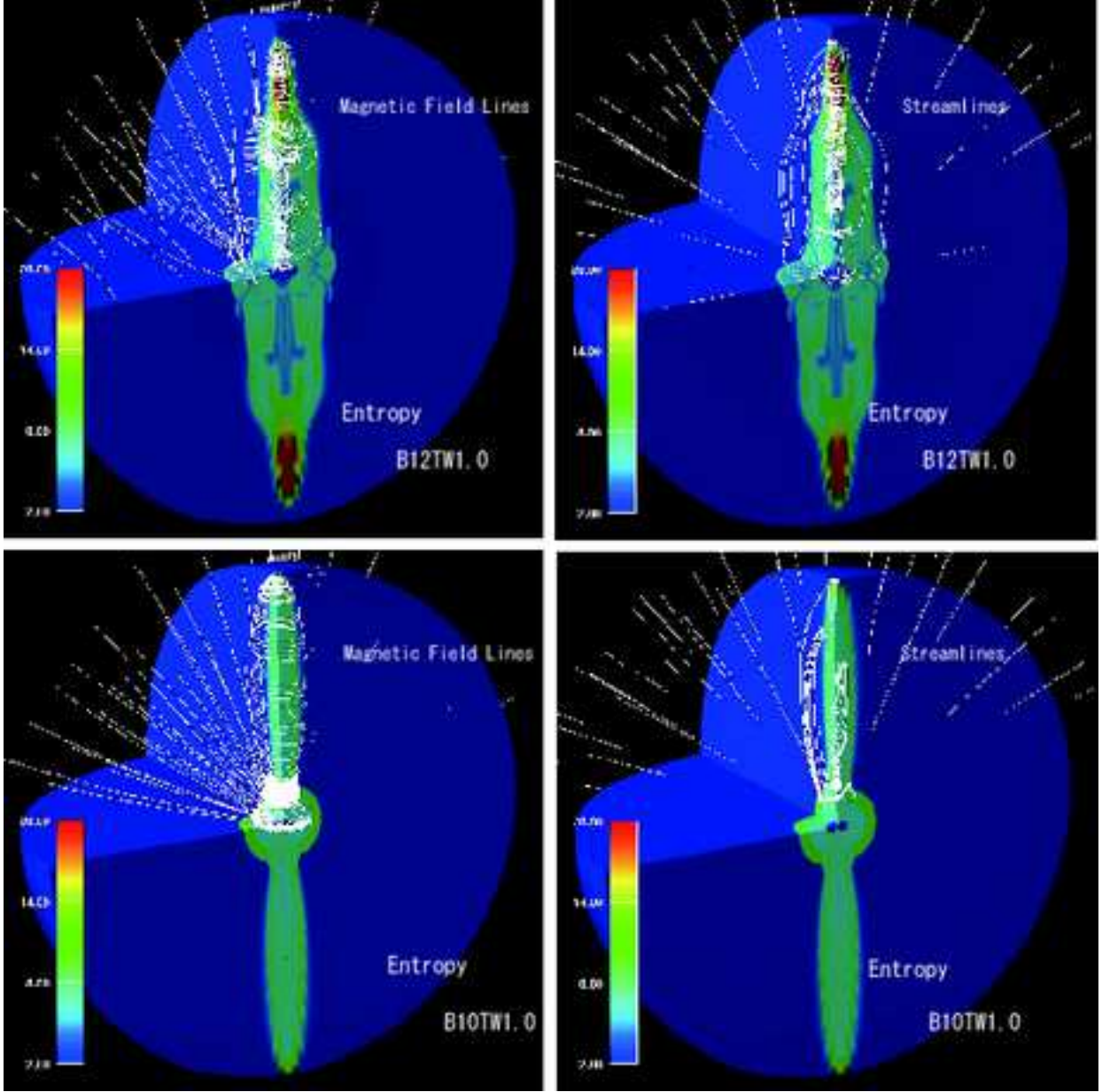


Fig. 4.— Three dimensional plots of entropy with the magnetic field lines (left) and the streamlines of the matter (right) during the jet propagation for models of B12TW1.0 (top) and B10TW1.0 (bottom), at 20 ms and 94 ms after bounce, respectively. The outer edge of the sphere colored by blue represents the radius of 7.5×10^7 cm. Note that the model of the top and bottom panel belongs to the prompt and delayed MHD exploding model, respectively. These panels highlight not only the wounded-up magnetic field around the rotational axis (left), but also the fallback of the matter from the head of the jet downwards to the equator, making a cocoon-like structure behind the jet (right).

Delayed MHD Exploding Model The models with weaker initial magnetic fields belong to the delayed MHD exploding model (see Figure 2). In the following, we explain their properties taking model B10TW1.0 as an example. It is noted again that this model has the same initial rotation rate with model B12TW1.0 of the previous section, but with the two orders-of-magnitudes weaker initial magnetic fields.

In the case of model B10TW1.0, the shock wave at bounce stalls in all directions at $\sim 1.5 \times 10^7$ cm. As shown in the top left panel of Figure 5, the plasma β is so high that the magnetic fields play no important role before bounce. After the shock stalls, the stalled shock begins to oscillate. The middle left and the bottom left panel shows the prolate and oblate phase during the oscillations, respectively. Until ~ 70 ms after bounce, the oscillation of the shock front continues diminishing its amplitude. Approximately the number of the oscillations is about 5 times this time. Without the magnetic fields, the oscillation should cease settling into the equilibrium state with the constant accretion through the stalled-shock to the center. However during this oscillation, the magnetic fields behind the stalled shock gradually grow due to the field wrapping and the plasma β around the polar regions becomes low as seen from the right side of the top right panel. Soon after the toroidal magnetic fields become as high as $\sim 10^{15}$ G behind the stalled shock (see the middle right panel), the stalled shock near the pole suddenly begins to propagate along the rotational axis and turns to be a collimated jet (see the bottom right panel). This revived jet does not stall in the iron-core. This is the reason why we call this model as the delayed MHD exploding model. The speed of the jet reaches about 5.5×10^9 cm/s (see the bottom right panel). Also in this jet, the toroidal component of the magnetic fields is dominant than the poloidal one and a fallback of the matter is found in the outer region of the jet (cocoon) as in the case of the promptly MHD exploding model (see the bottom two panels of Figure 4). At ~ 96 ms after bounce, the jet reaches $\sim 10^8$ cm. The explosion energy at that time reaches 0.094×10^{50} ergs.

As mentioned, the dynamical behaviors between the prompt and delayed MHD exploding models after bounce seem apparently different. However there are some important similarities between them, which we discuss from the next section.

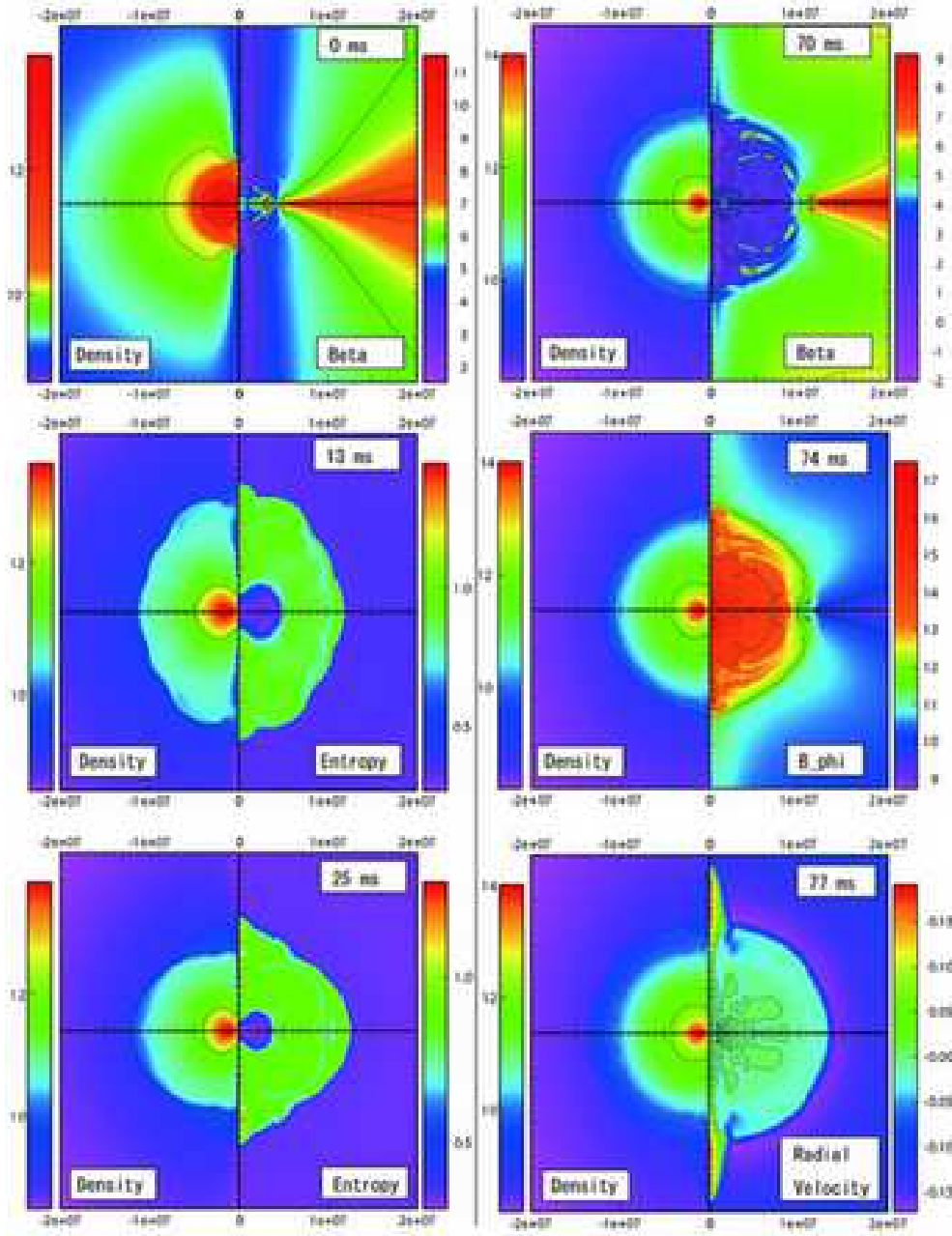


Fig. 5.— Same as Figure 3 but for model B10TW1.0, which is categorized to the delayed MHD exploding model. During the oscillations of the stalled shock after bounce (from middle left to bottom left), the magnetic fields behind the stalled shocks become large enough, due to the field wrapping (top and middle right), leading to the shock-revival for the formation of the magnetically-dominated jet (bottom right). Note that the unit of the horizontal and the vertical axis of all panels is in [cm].

5.3. Similarities of Prompt and Delayed MHD Exploding Model

In this section we focus on the similarities between the prompt and delayed MHD exploding models.

From Figure 6, it can be seen that the radial velocities and the magnetic fields of the jets are quite similar among the models regardless of the prompt or delayed exploding models. Typical values of the toroidal magnetic fields are $10^{14} - 10^{16}$ G and typical velocities are 10 – 30% of the speed of light. The opening angles of the jets are also similar. The width of this jet is about 8×10^6 cm when the jet reaches 7.5×10^7 cm, which means that the half opening angle of the jets is about 6° at this time. These characteristic values of the jets are summarized in Table 3.

Detailed properties of the jets are shown in Figures 7 and 8 to see the origin of these similarities. We fix the initial rotation rate and the initial field strength in Figure 7 and 8, respectively, to see their effects separately. In Figure 7, the initial rotation rate is $T/|W| = 1.0\%$ and the different lines correspond to the difference between the initial magnetic fields from 10^{12} (B12) to 10^{10} G (B10). In Figure 8, the initial magnetic field is 10^{11} G and the different lines corresponds the difference in the initial rotation rates.

From the top and middle panels of Figures 7 and 8, we find that the profiles of the toroidal magnetic field, the plasma β (0.1 – 0.01), the density, and the velocity, are rather similar behind the shock whose position can be seen from the discontinuity at ~ 700 km. Above all, it is surprising to see the remarkable similarity in the profiles of the toroidal magnetic fields behind the shock among the models (top left in Figures 7 and 8). The typical strength behind the shock is seen to be $\sim 10^{15}$ G. This critical strength of the toroidal magnetic field for the shock-revival is estimated as follows. The matter behind the stalled-shock is pushed inwards by the ram pressure of the accreting matter. This ram pressure is estimated as,

$$P = 4 \times 10^{28} \left(\frac{\rho}{10^{10} \text{g/cm}^3} \right) \left(\frac{\Delta v}{2 \times 10^9 \text{cm/s}} \right)^2 \text{erg/cm}^3, \quad (11)$$

where the typical density and the radial velocity are taken from Figure 1 and the bottom right panel of Figure 5, respectively. When the toroidal magnetic fields are amplified as large as $\sim 10^{15}$ G due to the field wrapping behind the shock, the resulting magnetic pressure, $\frac{B^2}{8\pi}$, can overwhelm the ram pressure, leading to the magnetic shock-revival. The origin of the similarity of the jets seen in Figure 3 comes from this mechanism. We find that this process works in all the computed models.

Moreover it is found that the poloidal fields behind the shock front do not depend on the initial rotation rate so much given the same initial field strength (bottom panels of Figure

8), while the difference of the poloidal magnetic fields behind the shock in the bottom panels of Figure 7 simply comes from the difference in the initial field strength. This feature is regardless of the prompt or delayed models.

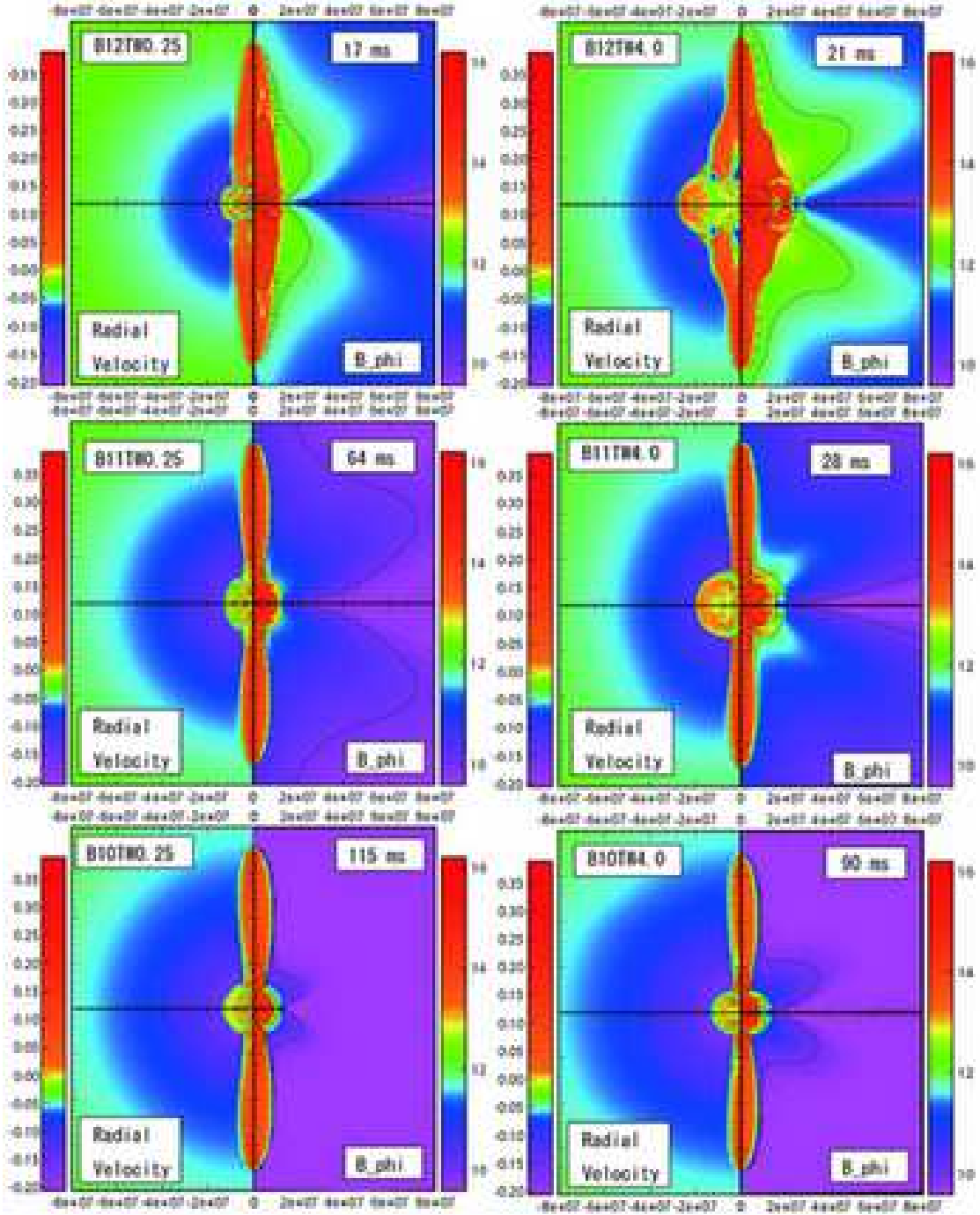


Fig. 6.— Contour of radial velocity (left side) and toroidal magnetic fields (right side in each panel) for various models, showing the similarity of the jets between the prompt and delayed MHD exploding models. The right and left panels correspond to the rapidly rotating ($T/|W| = 4.0\%$) and the slowly rotating $T/|W| = 0.25\%$ models, respectively. From top to bottom panels, the initial strength of the magnetic fields changes from strong (B12 models) to weak (B10 models). The time from bounce is shown in the top right part of each panel, indicating the difference between the prompt and the delayed models. Note that the unit of the horizontal and the vertical axis of all panels is in [cm].

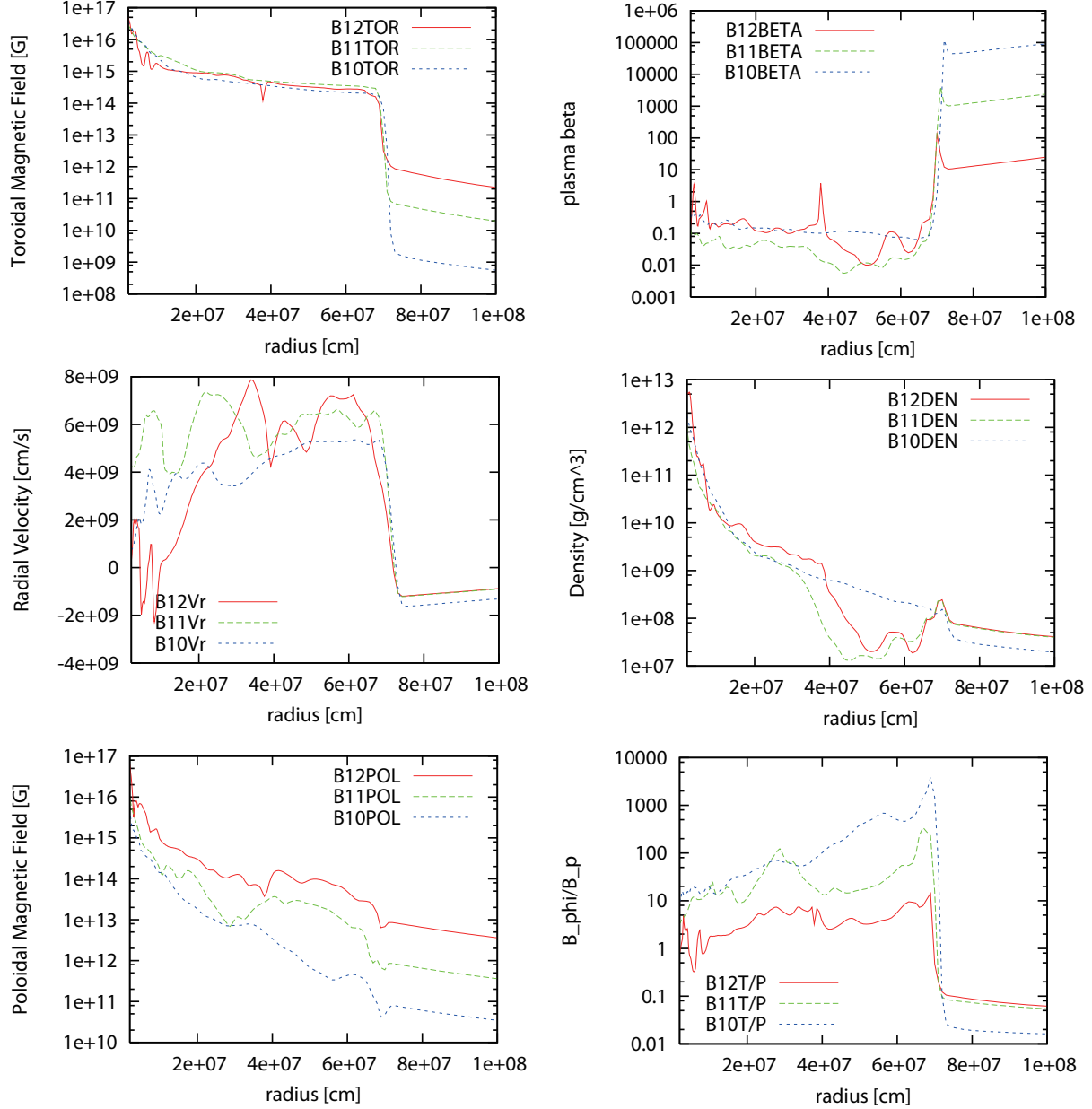


Fig. 7.— Various profiles of jets along the rotational axis, for models B12TW1.0 at 20 ms (solid), B11TW1.0 at 24 ms (short-dashed) and B10TW1.0 (dotted) at 94 ms after bounce, respectively, showing the effects of the difference of the initial magnetic fields (fixing the initial rotation rate of $T/|W| = 1.0\%$). Top left and right is the toroidal magnetic field (B_ϕ) and plasma beta ($\beta = P/\frac{B^2}{8\pi}$). Middle left and right is the radial velocity [cm/s] and the density [g/cm³]. Bottom left and right is the poloidal magnetic field (B_p) and the ratio of toroidal to poloidal magnetic field (B_ϕ/B_p). Note that the shock position is approximately 700 km as seen from the discontinuity of these profiles.

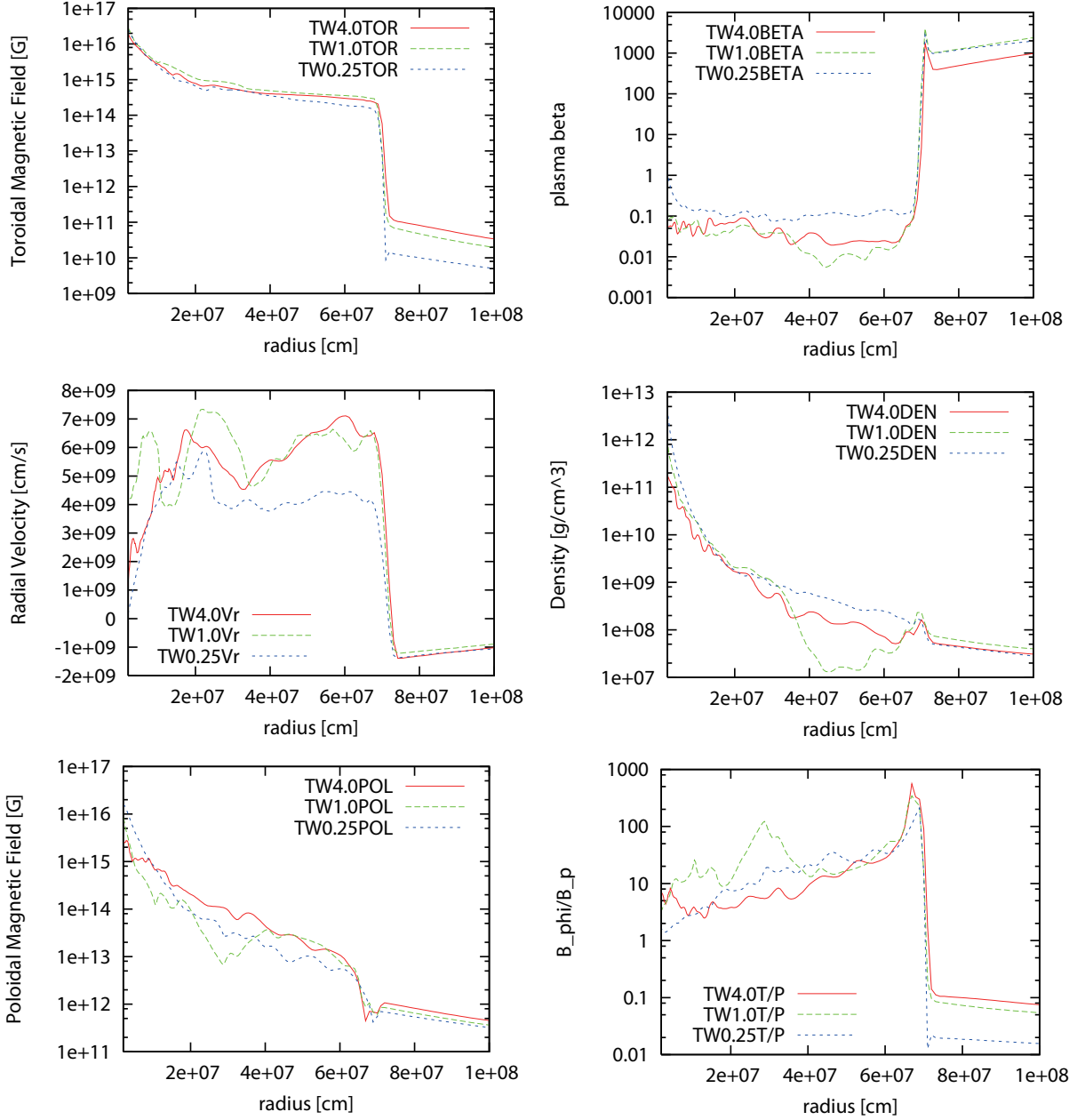


Fig. 8.— Same as Figure 7, but for models B11TW4.0 at 28 ms (solid), B11TW1.0 at 24 ms (short-dashed), and B11TW0.25 (dotted) at 64 ms after bounce, respectively, showing the effects of the difference of the initial rotation rates (fixing the initial field strength of B11).

Table 3: Characteristic properties of jets

Name	t_{exp} [ms]	$t_{1000\text{km}}$ [ms]	v_{jet} [cm/s]	$E_{\text{exp}1000\text{km}}$ [10^{50} ergs]
B12TW0.25	0	32	6.0×10^9	1.3
B11TW0.25	48	72	3.7×10^9	0.05
B10TW0.25	92	122	3.8×10^9	0.02
B12TW1.0	0	20	8.0×10^9	1.4
B11TW1.0	10	27	8.0×10^9	0.23
B10TW1.0	70	96	5.5×10^9	0.094
B12TW4.0	0	25	6.0×10^9	1.0
B11TW4.0	16	32	6.0×10^9	0.10
B10TW4.0	65	104	5.5×10^9	0.006

Note. — Properties of the jets. t_{exp} is the duration from bounce to the revival of the stalled shock due to the field wrapping. $t_{1000\text{km}}$ represents the duration required for the jet to reach $\sim 1000\text{km}$ after bounce. Explosion energy, $E_{\text{exp}1000\text{km}}$, and the jet velocity, v_{jet} is estimated at the moment. $E_{\text{exp}1000\text{km}}$ are normalized as 10^{50}erg . For the definition of the explosion energy, see Eq. (12).

5.4. Dependence of Initial Rotation Rates and Magnetic Field Strengths on Jet Arrival Times and Explosion Energies

In the previous section, we discuss the similarity among the computed models. From this section, we move on to discuss the differences among them.

Jet Arrival Time First we discuss the “jet arrival time” shown in Table 2, which is the timescale when the jet reaches the outer edge of the iron core of $\sim 1000\text{km}$. As discussed in the previous section, this timescale is mainly determined how long it takes for the magnetic fields behind the shock to become as large as the critical toroidal magnetic fields ($\sim 10^{15}\text{G}$) as a result of the field wrapping.

From the top left panel of Figure 9, it is seen that the strong initial magnetic fields shorten the jet arrival time. This tendency is seen in all the computed model regardless of the prompt or delayed exploding models. When the initial magnetic fields are strong enough ($\sim 10^{-4}$ of the gravitational energy), the jet arrival times between the different initial rotational models become almost the same. In this case, the critical magnetic fields for the shock-revival are already generated by the compression before core bounce. So the strong magneto-driven jets can produce the prompt MHD explosions in a similar way. For the rapidly rotating models (the sequence of TW1.0 and TW4.0), it is seen that the decrease in the rate of the jet arrival time as a function of the initial $E_m/|W|$ becomes smaller when the initial $E_m/|W|$ is larger than $\sim 10^{-6}$ (see the kink in the panel). This is because too strong magnetic fields transport the angular momentum of the protoneutron star outwards, leading to the suppression of the efficiency of the field wrapping after bounce.

In the top right panel of Figure 9, the dependence of the initial rotation rate on the jet arrival time is shown. By intuition, the jet arrival time may become shorter as the initial rotation rates become larger since the field-wrapping should become more efficient. The panel shows that this is true for moderately rotating models of the initial $T/|W|$ less than 0.01, but not true for the more rapidly rotating models. This can be explained as follows. Too rapid rotation of the core hinders the central core from collapsing due to the stronger centrifugal forces. This feature is clearly shown in the middle left panel of Figure 9 showing the density profiles. The density near the center is ~ 100 times lower than that for the slowly rotating models. Consequently, the inner core cannot gain much angular momentum by compression before the core-bounce as seen in the middle panels of Figure 9. It is noted here again that the angular velocity is well conserved before the core-bounce and distributed following the density (see section 4.1). Reflecting these aspects, the amplification rate of the magnetic fields ($\frac{dE_m}{dt}/E_m$) near core-bounce becomes smaller for the most rapidly rotating model (TW4.0) as seen from the bottom panel of Figure 9. This suppression makes the jet

arrival time almost constant or longer as the initial $T/|W|$ becomes larger than ~ 0.01 as in the top right panel of Figure 9.

Explosion Energies In addition to a wide variety of the jet arrival times, we find a large difference in the strengths of the magnetic explosions.

As a measure of the strength, we define the explosion energy as,

$$E_{\text{exp1000km}} = \int_D \mathbb{V} e_{\text{local}} = \int_D \mathbb{V} (e_{\text{kin}} + e_{\text{int}} + e_{\text{mag}} + e_{\text{grav}}), \quad (12)$$

here e_{local} is the sum of e_{kin} , e_{int} , e_{mag} and e_{grav} , with being the kinetic, internal, magnetic, and gravitational energy, respectively (see Appendix A.1 for their definitions in special relativity) and D represents the domain where the local energy is positive, indicating that the matter is not bound by the gravity. The explosion energy is evaluated when the jet arrives at the radius of 1000km at the polar direction. The value of the explosion energy is summarized in Figure 10. Generally speaking, it is found that the explosion energies becomes larger for the prompt MHD exploding models (red) than the delayed MHD exploding models (green).

What makes the difference on the explosion energies? Figure 11 shows the toroidal magnetic fields (left side) and the local energy (right side) in the jets from the stronger to the weak magnetic fields models (from top to bottom panels). It is seen that the regions where the local energy is positive mostly coincide with the regions where the strong toroidal magnetic fields are generated. As the initial field strength becomes larger, the regions where the local energy become positive becomes larger, leading to the larger explosion energies. In the case of the delayed exploding model, it is found that the width of the jets becomes narrower, which results in the smaller explosion energies. Although the properties of the jets just on the rotational axis are similar among the models seen from Figures 7 and 8, the lateral structures of the jets is found to have influence over the explosion energies.

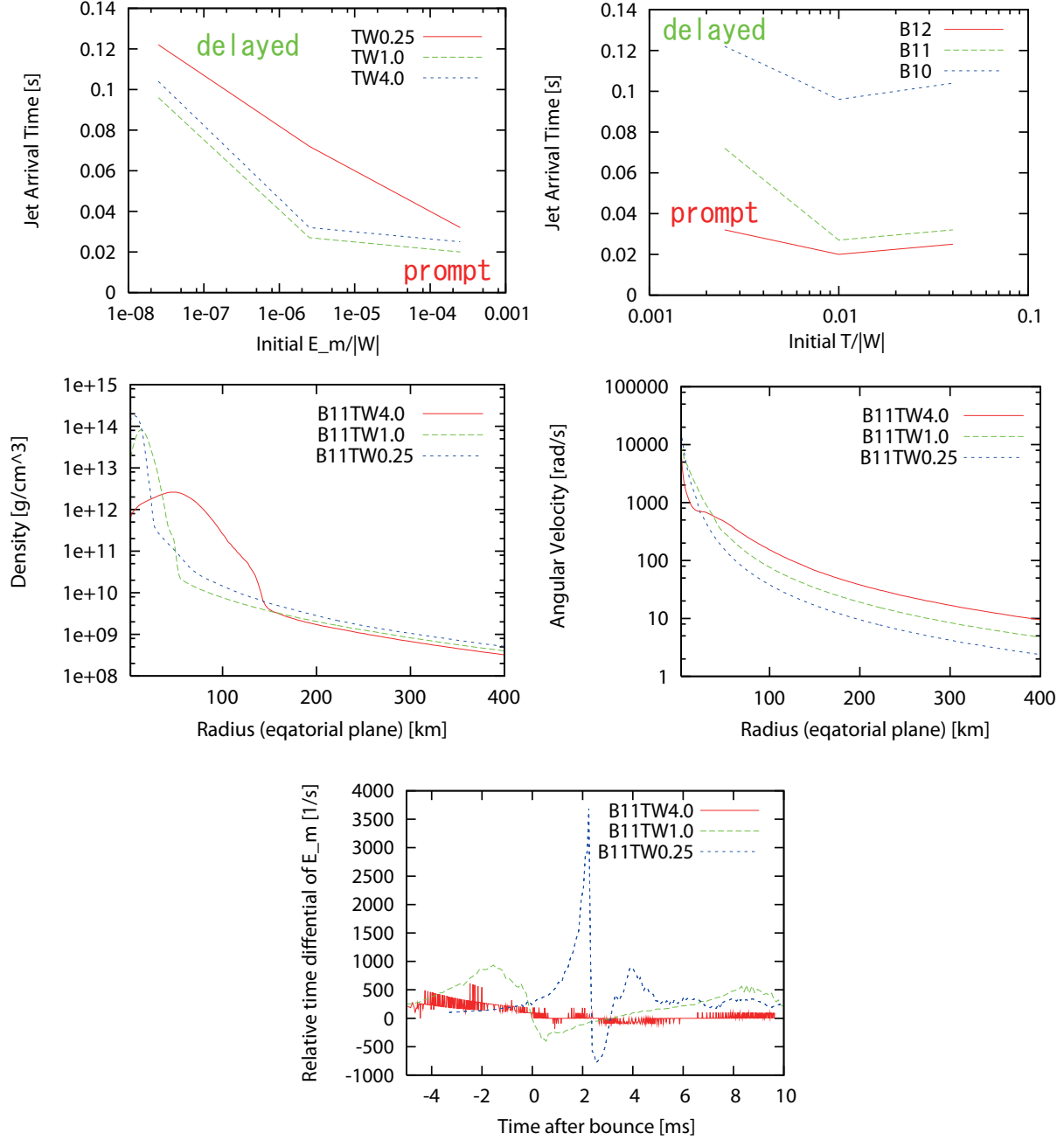


Fig. 9.— Dependence of the initial magnetic field strength (top left) and of the initial rotation rate (top right) on the jet arrival time. Here $E_m/|W|$ and $T/|W|$ represent the ratio of initial magnetic and rotational energies to the gravitational energy, respectively. The jet arrival time is the duration for the jet to reach the outer edge of iron core of ~ 1000 km. Middle left and right panel shows the distribution of the density and the angular velocity for models B11TW4.0, B11TW1.0 and B11TW0.25 at core bounce as a function of the equatorial radius, respectively. Bottom panel shows the temporal amplification rate ($\frac{dE_m}{dt}/E_m$) near core bounce.

		$T/ W (\%)$		
		0.25%	1.0%	4.0%
$B_0(\text{Gauss})$	10^{10}G	0.02	0.094	0.006
	10^{11}G	0.05	0.23	0.010
	10^{12}G	1.3	1.4	1.0

Fig. 10.— The explosion energy for all the models. The energies are normalized to 10^{50}erg . Note again that the red and green blocks indicate the prompt and delayed MHD exploding models, respectively. See Eq. (12) for the definition of the explosion energy.

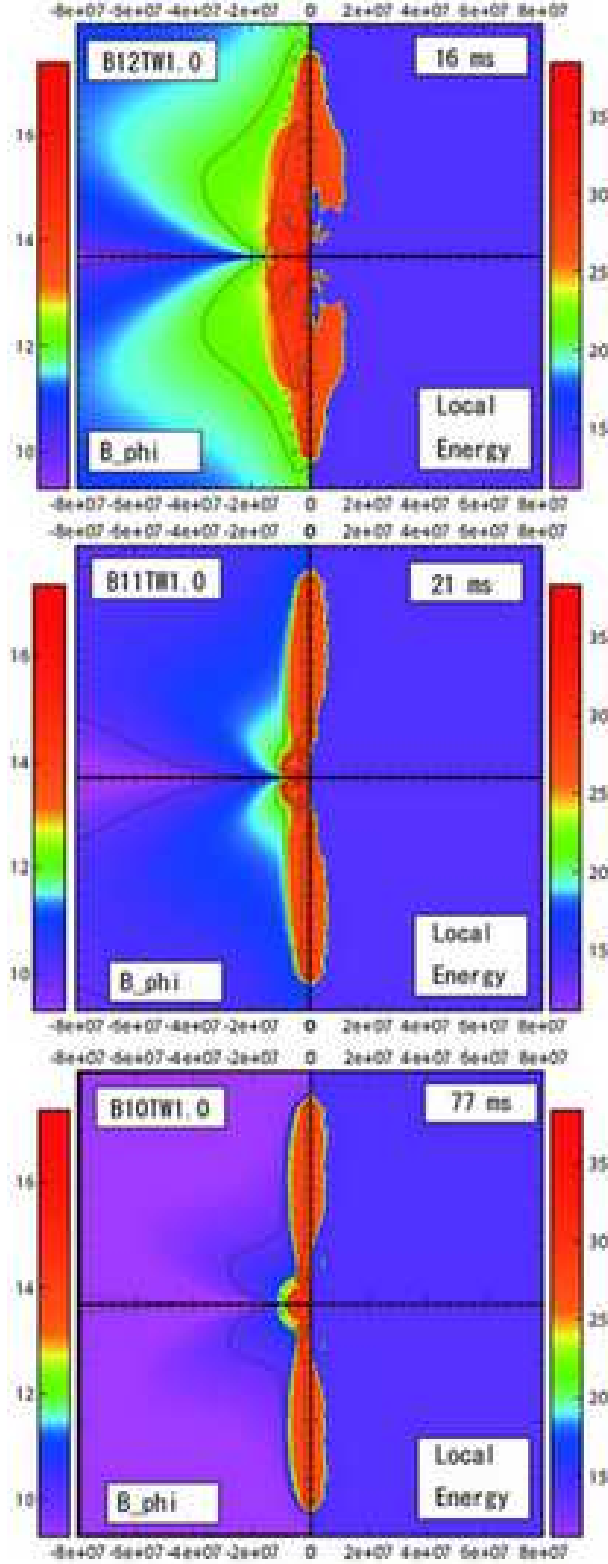


Fig. 11.— Contour of toroidal magnetic field and the local energy for models B12TW1.0, B11TW1.0 and B10TW1.0, near the shock break-out. In each panels, the logarithm of toroidal magnetic field[G] (left side) and the logarithm of local energy [ergs/cm^3] (right side) is shown, respectively. It should be noted that negative local energy is colored by purple and that the negative local energy is removed from the model shown. Note that the unit of the

6. Summary and Discussion

We performed a series of two-dimensional MHD simulations of rotational core-collapse of magnetized massive stars. The main motivation was to clarify how the strong magnetic fields and the rapid rotation of the core affect the magnetic explosions. To handle the very strong magnetic fields, we developed a new code under the framework of special relativity. A novel point is that the microphysics such as the realistic equation of state and the neutrino coolings is implemented to the special relativistic MHD code. Due to these advantages, our computation can achieve a longer time-stretch of the evolutions compared to previous studies. The obtained results can be summarized as follows.

- Magnetically powered jets are commonly found in all the computed models. In the jets, the magnetic fields are dominated by the toroidal components as a result of the field wrapping. For the profiles and strengths of the toroidal fields behind the jets, we find a remarkable similarity. We find that the jet-like explosions occur when the magnetic pressure behind the shock becomes strong, due to the field wrapping, enough to overwhelm the ram pressure of the accreting matter. The required toroidal magnetic fields are similar of $\sim 10^{15}\text{G}$, which can be also understood by a simple order-of-magnetite estimation. Reflecting the similarity in the mechanism of producing jets, global properties of the jets such as the velocities ($\sim 20\%$ of the speed of light) and the opening angles ($\sim 6^\circ$) are also found to be similar among the computed models.
- The timescale before the onset of the magnetic shock-revival are quite different depending on the initial strengths of rotation and magnetic fields. When the initial strengths of rotation and magnetic field are larger, the jet can be launched just after the core-bounce, which we called as the promptly MHD exploding models. We furthermore find that even for the model with the weaker initial field and slow rotation, the jet-like explosions can occur after sufficient field wrapping to reach the critical field strength, which we called as the delayed MHD exploding models. In this case, the explosion can be delayed about $\sim 100\text{ms}$ after bounce. The explosion energy also strongly depends on the the time difference before the shock-revival. The stronger initial magnetic fields make wider exploding regions, leading to the larger explosion energy. The largest MHD-driven explosion energy obtained is $\sim 10^{50}\text{ erg}$.

A role of the shock-revival as a result of the field wrapping was also pointed out in the analytic studies by Uzdensky & MacFadyen (2007a,b). Our numerical simulations are in favor of their expectations. In addition, our simulations show that the explosion energy becomes smaller than the estimated ones in their studies because the magnetic tower cannot be wider as they assumed. Thus the highly relativistic outflows of the GRBs seems to be

hardly explained by the jets obtained in our computations. As discussed in the final part of this section, we think that the jet might be good for the explanation of the X-ray flashes.

As for our numerical computations, we shall address a few imperfections. Magneto-rotational Instability (MRI) has been pointed out to be active in the outer layer of protoneutron star which rotates strongly differentially (Akiyama et al. 2003; Kotake et al. 2004a; Masada et al. 2006). The wavelength of maximum growth rate of the linear instability, $\lambda = \frac{2\pi v_a}{\Omega}$, becomes $\sim 5 \left(\frac{300 \text{s}^{-1}}{\Omega} \right) \left(\frac{B}{10^{12} \text{G}} \right) \left(\frac{10^{10} \text{g/cm}^3}{\rho} \right)^{1/2} \text{km}$ (Balbus & Hawley 1998), where our numerical grid is $\sim 3 \text{km}$ there. Since 10 – 100 times finer mesh than the wavelength is required for resolving the MRI (Shibata et al. 2006), our simulations are insufficient to take into account the field amplification due to the MRI. This is an very important task remained to be investigated, although the computational costs are still expensive. As for the micro-physics, the neutrino heating is not included as Burrows et al. (2007). Since the timescale for the magnetic explosions in the polar direction are much earlier than the neutrino heating or the g-mode excited explosions, we think that both of them basically should play a minor role here. On the other hand, the neutrino heating could be helpful for producing the explosion in the direction of the equatorial plane where the field-wrapping induced magnetic explosions are unlikely to occur. Finally the general relativistic (GR) effects are not incorporated in our simulations. During our simulation time, the central protoneutron stars do not collapse to the black holes as inferred from a simple estimation of the Schwarzschild radius. Thus we think that the GR effect may not drastically change our results qualitatively.

Bearing these caveats in mind, we state some speculations based on our results. The protoneutron stars obtained here are with the poloidal magnetic fields of order 10^{15}[G] and with its rotation period of an order of milliseconds, which could be the origin of the magnetar according to a hypothesis by Duncan & Thompson (1992). If so, it means that the magnetically-driven jets could be associated with the formation of the magnetars. Our results suggest that the toroidal component of the magnetic fields are dominant in the young magnetars. The large magnetic energy of the toroidal component stored in deep crusts and cores of the magnetars would be transported outside via Alfvén waves and be released as giant-flares of the SGRs (Duncan & Thompson 1992; Thompson & Duncan 2001; Thompson et al. 2002). Some observational evidences support this picture. For example, quasi periodic oscillations discovered in a X-ray light curve of the giant-flare from SGR1806-20 would originate from the Alfvén wave from the interior of the star (Rea et al. 2006; Israel et al. 2005). There are several studies indicating that the magnetar formation yields the XRF (Mazzali et al. 2006; Maeda et al. 2007a,b). While the ordinary GRBs require the highly relativistic ejecta, the mildly relativistic ejecta is favorable for XRFs (Toma et al. 2007; Soderberg et al. 2006; Ghisellini et al. 2007), which may be the case here because the magneto-driven jets become

only mildly relativistic due to the high baryon loading of the matter along the rotational axis.

There remain more rooms to be investigated applying our simulations. In this study, we employed one progenitor model. Since the accretion rate of the matter to the protoneutron stars should depend on the progenitor mass (Heger et al. 2005; Woosley & Heger 2006), we think it very important to investigate how the criterion of the magnetic shock-revival changes with the progenitor models. Moreover the initial configurations of the magnetic fields, which is still highly uncertain, could be changed in a systematic manner like in Sawai et al. (2005, 2007), to see their effects on dynamics. While this study focussed on the shock-propagation in the iron cores, we plan to continue to follow the dynamics later on (phase 4 in the introduction). Very recent studies by Komissarov & Barkov (2007); Bucciantini et al. (2007) are on this line. Our simulation can be more consistent than their studies in the sense that we start the simulations from the onset of the core-collapse, and that the protoneutron stars are not excised like their models. By continuing the simulations of the jet propagations till the shock-breakout, we plan to study the possible connection between the magnetically-driven jets obtained here and the origins of the XRFs in the forthcoming work (Takiwaki et al. in preparation).

We are grateful to S. Yamada for fruitful discussions. KK thanks to E. Müller for useful discussions. TT is grateful to S. Horiuchi for proofreading the manuscript. Numerical computations were in part carried on VPP5000 and general common use computer system at the center for Computational Astrophysics, CfCA, the National Astronomical Observatory of Japan. This study was partially supported by Grants-in-Aid for the Scientific Research from the Ministry of Education, Science and Culture of Japan through No.S 19104006, No. 14079202 and No. 16740134.

REFERENCES

- Akiyama, S., Wheeler, J. C., Meier, D. L., & Lichtenstadt, I. 2003, *ApJ*, 584, 954
- Aloy, M. A., Müller, E., Ibáñez, J. M., Martí, J. M., & MacFadyen, A. 2000, *ApJ*, 531, L119
- Anninos, P., Fragile, P. C., & Murray, S. D. 2003, *ApJS*, 147, 177
- Balbus, S. A. & Hawley, J. F. 1998, *Reviews of Modern Physics*, 70, 1
- Brio, M. & Wu, C. C. 1988, *Journal of Computational Physics*, 75, 400

- Bucciantini, N., Quataert, E., Arons, J., Metzger, B. D., & Thompson, T. A. 2007, MNRAS, L126+
- Burrows, A., Dessart, L., Livne, E., Ott, C. D., & Murphy, J. 2007, ApJ, 664, 416
- Cerdá-Durán, P., Font, J. A., & Dimmelmeyer, H. 2007, ArXiv Astrophysics e-prints
- De Villiers, J.-P., Hawley, J. F., & Krolik, J. H. 2003, ApJ, 599, 1238
- De Villiers, J.-P., Hawley, J. F., Krolik, J. H., & Hirose, S. 2005, ApJ, 620, 878
- Duncan, R. C. & Thompson, C. 1992, ApJ, 392, L9
- Epstein, R. I. & Pethick, C. J. 1981, ApJ, 243, 1003
- Fujimoto, S.-i., Kotake, K., Yamada, S., Hashimoto, M.-a., & Sato, K. 2006, ApJ, 644, 1040
- Fuller, G. M., Fowler, W. A., & Newman, M. J. 1985, ApJ, 293, 1
- Galama, T. J., Vreeswijk, P. M., van Paradijs, J., Kouveliotou, C., Augusteijn, T., Böhnhardt, H., Brewer, J. P., Doublier, V., Gonzalez, J.-F., Leibundgut, B., Lidman, C., Hainaut, O. R., Patat, F., Heise, J., in’t Zand, J., Hurley, K., Groot, P. J., Strom, R. G., Mazzali, P. A., Iwamoto, K., Nomoto, K., Umeda, H., Nakamura, T., Young, T. R., Suzuki, T., Shigeyama, T., Koshut, T., Kippen, M., Robinson, C., de Wildt, P., Wijers, R. A. M. J., Tanvir, N., Greiner, J., Pian, E., Palazzi, E., Frontera, F., Masetti, N., Nicastro, L., Feroci, M., Costa, E., Piro, L., Peterson, B. A., Tinney, C., Boyle, B., Cannon, R., Stathakis, R., Sadler, E., Begam, M. C., & Ianna, P. 1998, Nature, 395, 670
- Gavriil, F. P., Kaspi, V. M., & Woods, P. M. 2002, Nature, 419, 142
- Ghisellini, G., Ghirlanda, G., & Tavecchio, F. 2007, MNRAS, L117+
- Harding, A. K. & Lai, D. 2006, Reports of Progress in Physics, 69, 2631
- Hawley, J. F. & Krolik, J. H. 2006, ApJ, 641, 103
- Hawley, J. F., Smarr, L. L., & Wilson, J. R. 1984a, ApJ, 277, 296
- . 1984b, ApJS, 55, 211
- Heger, A. & Langer, N. 2000, ApJ, 544, 1016
- Heger, A., Woosley, S. E., & Spruit, H. C. 2005, ApJ, 626, 350

- Ibrahim, A. I., Swank, J. H., & Parke, W. 2003, *ApJ*, 584, L17
- Israel, G. L., Belloni, T., Stella, L., Rephaeli, Y., Gruber, D. E., Casella, P., Dall’Osso, S., Rea, N., Persic, M., & Rothschild, R. E. 2005, *ApJ*, 628, L53
- Itoh, N., Adachi, T., Nakagawa, M., Kohyama, Y., & Munakata, H. 1989, *ApJ*, 339, 354
- . 1990, *ApJ*, 360, 741
- Janka, H.-T., Langanke, K., Marek, A., Martínez-Pinedo, G., & Müller, B. 2007, *Phys. Rep.*, 442, 38
- Koide, S., Shibata, K., & Kudoh, T. 1998, *ApJ*, 495, L63+
- Komissarov, S. S. & Barkov, M. V. 2007, *MNRAS*, 382, 1029
- Komissarov, S. S. & McKinney, J. C. 2007, *MNRAS*, 377, L49
- Kotake, K., Sato, K., & Takahashi, K. 2006, *Reports of Progress in Physics*, 69, 971
- Kotake, K., Sawai, H., Yamada, S., & Sato, K. 2004a, *ApJ*, 608, 391
- Kotake, K., Yamada, S., & Sato, K. 2003, *ApJ*, 595, 304
- Kotake, K., Yamada, S., Sato, K., Sumiyoshi, K., Ono, H., & Suzuki, H. 2004b, *Phys. Rev. D*, 69, 124004
- Krolik, J. H., Hawley, J. F., & Hirose, S. 2005, *ApJ*, 622, 1008
- Lattimer, J. M. & Prakash, M. 2007, *Phys. Rep.*, 442, 109
- Leismann, T., Antón, L., Aloy, M. A., Müller, E., Martí, J. M., Miralles, J. A., & Ibáñez, J. M. 2005, *A&A*, 436, 503
- MacFadyen, A. I. & Woosley, S. E. 1999, *ApJ*, 524, 262
- Maeda, K., Kawabata, K., Tanaka, M., Nomoto, K., Tominaga, N., Hattori, T., Minezaki, T., Kuroda, T., Suzuki, T., Deng, J., Mazzali, P. A., & Pian, E. 2007a, *ApJ*, 658, L5
- Maeda, K., Tanaka, M., Nomoto, K., Tominaga, N., Kawabata, K., Mazzali, P. A., Umeda, H., Suzuki, T., & Hattori, T. 2007b, *ApJ*, 666, 1069
- Masada, Y., Sano, T., & Takabe, H. 2006, *ApJ*, 641, 447
- Matt, S., Frank, A., & Blackman, E. G. 2006, *ApJ*, 647, L45

- Mazzali, P. A., Deng, J., Nomoto, K., Sauer, D. N., Pian, E., Tominaga, N., Tanaka, M., Maeda, K., & Filippenko, A. V. 2006, *Nature*, 442, 1018
- McKinney, J. C. & Narayan, R. 2007, *MNRAS*, 375, 531
- Meszaros, P. 2006, *Reports of Progress in Physics*, 69, 2259
- Mizuno, Y., Hardee, P., & Nishikawa, K.-I. 2007, *ApJ*, 662, 835
- Mizuno, Y., Nishikawa, K.-I., Koide, S., Hardee, P., & Fishman, G. J. 2006, *ArXiv Astrophysics e-prints*
- Mizuta, A., Yamasaki, T., Nagataki, S., & Mineshige, S. 2006, *ApJ*, 651, 960
- Moiseenko, S. G., Bisnovatyi-Kogan, G. S., & Ardeljan, N. V. 2006, *MNRAS*, 370, 501
- Nagataki, S., Takahashi, R., Mizuta, A., & Takiwaki, T. 2007, *ApJ*, 659, 512
- Nishikawa, K.-I., Richardson, G., Koide, S., Shibata, K., Kudoh, T., Hardee, P., & Fishman, G. J. 2005, *ApJ*, 625, 60
- Nishimura, S., Kotake, K., Hashimoto, M.-a., Yamada, S., Nishimura, N., Fujimoto, S., & Sato, K. 2006, *ApJ*, 642, 410
- Obergaulinger, M., Aloy, M. A., Dimmelmeyer, H., & Müller, E. 2006, *A&A*, 457, 209
- Paczynski, B. 1998, *ApJ*, 494, L45+
- Piran, T. 1999, *Phys. Rep.*, 314, 575
- Piro, L., Amati, L., Antonelli, L. A., Butler, R. C., Costa, E., Cusumano, G., Feroci, M., Frontera, F., Heise, J., in 't Zand, J. J. M., Molendi, S., Muller, J., Nicastro, L., Orlandini, M., Owens, A., Parmar, A. N., Soffitta, P., & Tavani, M. 1998, *A&A*, 331, L41
- Proga, D., MacFadyen, A. I., Armitage, P. J., & Begelman, M. C. 2003, *ApJ*, 599, L5
- Rea, N., Israel, G. L., Mereghetti, S., Tiengo, A., Zane, S., Turolla, R., & Stella, L. 2006, *Chinese Journal of Astronomy and Astrophysics Supplement*, 6, 155
- Rea, N., Israel, G. L., Stella, L., Oosterbroek, T., Mereghetti, S., Angelini, L., Campana, S., & Covino, S. 2003, *ApJ*, 586, L65
- Rosswog, S. & Liebendörfer, M. 2003, *MNRAS*, 342, 673

- Savaglio, S., Glazebrook, K., & Le Borgne, D. 2006, in American Institute of Physics Conference Series, Vol. 836, Gamma-Ray Bursts in the Swift Era, ed. S. S. Holt, N. Gehrels, & J. A. Nousek, 540–545
- Sawai, H., Kotake, K., & Yamada, S. 2005, *ApJ*, 631, 446
- . 2007, *ArXiv*, 709.1795
- Scheidegger, S., Fischer, T., & Liebendoerfer, M. 2007, *ArXiv e-prints*, 709.0168
- Sekiguchi, Y. & Shibata, M. 2007, *Progress of Theoretical Physics*, 117, 1029
- Shapiro, S. L. & Teukolsky, S. A. 1983, Black holes, white dwarfs, and neutron stars: The physics of compact objects (Research supported by the National Science Foundation. New York, Wiley-Interscience, 1983, 663 p.)
- Shen, H., Toki, H., Oyamatsu, K., & Sumiyoshi, K. 1998, *Nuclear Physics A*, 637, 435
- Shibata, M., Liu, Y. T., Shapiro, S. L., & Stephens, B. C. 2006, *Phys. Rev. D*, 74, 104026
- Sod, G. A. 1978, *Journal of Computational Physics*, 27, 1
- Soderberg, A. M., Kulkarni, S. R., Nakar, E., Berger, E., Cameron, P. B., Fox, D. B., Frail, D., Gal-Yam, A., Sari, R., Cenko, S. B., Kasliwal, M., Chevalier, R. A., Piran, T., Price, P. A., Schmidt, B. P., Pooley, G., Moon, D.-S., Penprase, B. E., Ofek, E., Rau, A., Gehrels, N., Nousek, J. A., Burrows, D. N., Persson, S. E., & McCarthy, P. J. 2006, *Nature*, 442, 1014
- Spruit, H. C. 2002, *A&A*, 381, 923
- Stanek, K. Z., Gnedin, O. Y., Beacom, J. F., Gould, A. P., Johnson, J. A., Kollmeier, J. A., Modjaz, M., Pinsonneault, M. H., Pogge, R., & Weinberg, D. H. 2006, *Acta Astronomica*, 56, 333
- Stanek, K. Z., Matheson, T., Garnavich, P. M., Martini, P., Berlind, P., Caldwell, N., Challis, P., Brown, W. R., Schild, R., Krisciunas, K., Calkins, M. L., Lee, J. C., Hathi, N., Jansen, R. A., Windhorst, R., Echevarria, L., Eisenstein, D. J., Pindor, B., Olszewski, E. W., Harding, P., Holland, S. T., & Bersier, D. 2003, *ApJ*, 591, L17
- Stone, J. M. & Hardee, P. E. 2000, *ApJ*, 540, 192
- Stone, J. M. & Norman, M. L. 1992, *ApJS*, 80, 753
- Suwa, Y., Takiwaki, T., Kotake, K., & Sato, K. 2007a, *ApJ*, 665, L43

- . 2007b, ArXiv e-prints, 704
- Symbalisty, E. M. D. 1984, ApJ, 285, 729
- Takahashi, K., El Eid, M. F., & Hillebrandt, W. 1978, A&A, 67, 185
- Takiwaki, T., Kotake, K., Nagataki, S., & Sato, K. 2004, ApJ, 616, 1086
- Thompson, C. & Duncan, R. C. 2001, ApJ, 561, 980
- Thompson, C., Lyutikov, M., & Kulkarni, S. R. 2002, ApJ, 574, 332
- Thompson, T. A., Chang, P., & Quataert, E. 2004, ApJ, 611, 380
- Toma, K., Ioka, K., Sakamoto, T., & Nakamura, T. 2007, ApJ, 659, 1420
- Usov, V. V. 1992, Nature, 357, 472
- Uzdensky, D. A. & MacFadyen, A. I. 2007a, ApJ, 669, 546
- . 2007b, Physics of Plasmas, 14, 6506
- van Leer, B. 1977, Journal of Computational Physics, 23, 276
- Wheeler, J. C., Yi, I., Höflich, P., & Wang, L. 2000, ApJ, 537, 810
- Woosley, S. E. & Heger, A. 2006, ApJ, 637, 914
- Yamada, S. & Sawai, H. 2004, ApJ, 608, 907
- Zhang, B. & Harding, A. K. 2000, ApJ, 535, L51
- Zhang, W., Woosley, S. E., & MacFadyen, A. I. 2003, ApJ, 586, 356

A. Derivation of the Basic Equations for SRMHD

In this Appendix, we summarize formalisms on the basic equations and the numerical tests for our newly developed SRMHD code. For the formalisms, we follow the derivation of De Villiers et al. (2003); Hawley et al. (1984a,b). For convenience, we proceed the derivation keeping the metric general forms, i.e.,

$$g_{\mu\nu} = \begin{pmatrix} -\alpha & \beta_i \\ \beta_j & \gamma_{ij} \end{pmatrix}. \quad (\text{A1})$$

where α is the lapse function, β is the shift vector and γ_{ij} is the spatial 3-metric. And we take the Minkowski metric later.

There are four fundamental magnetohydrodynamic equations. The conservation of baryon number is

$$\partial_\mu \rho U^\mu = 0 \quad (\text{A2})$$

where ρ, U^μ ($\mu = 0, 1, 2, 3$) are baryon mass density and 4-velocity at each point. The conservation of the stress-energy is

$$\partial_\mu T^{\mu\nu} = 0 \quad (\text{A3})$$

where $T^{\mu\nu}$ is stress-energy tensor and Maxwell's equations

$$\partial_\mu F^{\mu\nu} = 4\pi J^\nu, \quad (\text{A4})$$

$$\partial_\mu {}^*F^{\mu\nu} = 0. \quad (\text{A5})$$

where $F^{\mu\nu}$ is the antisymmetric electro-magnetic tensor and

$${}^*F^{\mu\nu} = \frac{1}{2} \epsilon^{\mu\nu\delta\sigma} F_{\delta\sigma} \quad (\text{A6})$$

is dual of $F^{\mu\nu}$. Maxwell's equations are supplemented by the equation of the charge conservation $\partial_\mu J^\mu = 0$.

The energy momentum tensor consists of perfect fluid parts and electromagnetic parts, i.e.

$$T^{\mu\nu} = \rho h^* U^\mu U^\nu + p g^{\mu\nu} + \frac{1}{4\pi} \left(F^\mu{}_\alpha F^{\nu\alpha} - \frac{1}{4} F_{\alpha\beta} F^{\alpha\beta} g^{\mu\nu} \right) \quad (\text{A7})$$

where $h^* = (1 + e/\rho + p/\rho)$ is the relativistic enthalpy with e and p being the internal energy and the pressure, respectively.

For later convenience, we define magnetic induction in the rest frame of the fluid,

$$b^\mu = \frac{1}{\sqrt{4\pi}} {}^*F^{\mu\nu} U_\nu. \quad (\text{A8})$$

We adopt the ideal MHD limit and assume infinite conductivity (the flux-freezing condition), where in the electric field in the fluid rest frame is zero, i.e., $F_{\mu\nu} U^\nu = 0$.

Combining Eq. (A6) with (Eq. A8) and conditions for infinite conductivity, we obtain

$$F_{\mu\nu} = \epsilon_{\alpha\beta\mu\nu} \sqrt{4\pi} b^\alpha U^\beta. \quad (\text{A9})$$

The orthogonality condition

$$b^\mu U_\mu = 0 \quad (\text{A10})$$

follows directly from Eq. (A8).

The induction Eq. (A5) can also be rewritten by substituting the definitions,

$$\partial_\alpha (U^\alpha b^\beta - b^\alpha U^\beta) = 0. \quad (\text{A11})$$

By expanding this equation using the product rule and applying the orthogonality condition Eq. (A10), we obtain the identity

$$U_\nu b^\mu \nabla_\mu U^\nu = 0. \quad (\text{A12})$$

It is useful to rewrite the energy momentum tensor as

$$T^{\mu\nu} = (\rho h^* + |b|^2) U^\mu U^\nu + (p + \frac{|b|^2}{2}) g^{\mu\nu} - b^\mu b^\nu. \quad (\text{A13})$$

We have to expand basic equations in terms of the code variable, and transform the equation for auxiliary density, energy and momentum functions $D = \rho W, E = eW, S_i = \rho h W^2 v_i$. Finally the set of variables D, E, S_i, B_i will be evolved through the basic equations transformed here.

The equation of baryon conservation (A2) can be expanded in terms of the code variables easily,

$$\partial_t D + \frac{1}{\sqrt{\gamma}} \partial_j (D \sqrt{\gamma} V^j) = 0. \quad (\text{A14})$$

The equation of energy conservation is derived by contracting (A3) with U_ν ,

$$U_\nu \nabla_\mu T^{\mu\nu} = U_\nu \nabla_\mu \left\{ (\rho h^* + \|b\|^2) U^\mu U^\nu + \left(P + \frac{\|b\|^2}{2} \right) g^{\mu\nu} - b^\mu b^\nu \right\} = 0. \quad (\text{A15})$$

By using the identity (A12) and (A2), we obtain the local energy conservation

$$\nabla_\mu (\rho \epsilon U^\mu) + P \nabla_\mu U^\mu = 0, \quad (\text{A16})$$

Applying the definition for the auxiliary energy function E , the energy equation is rewritten as follows:

$$\partial_t (E) + \frac{1}{\sqrt{\gamma}} \partial_i (\sqrt{\gamma} E V^i) + P \partial_t (W) + \frac{P}{\sqrt{\gamma}} \partial_i (\sqrt{\gamma} W V^i) = 0. \quad (\text{A17})$$

The momentum conservation equations follow from

$$\nabla_\mu T^\mu_\nu = \nabla_\mu \left\{ (\rho h^* + \|b\|^2) U^\mu U_\nu + \left(P + \frac{\|b\|^2}{2} \right) \delta^\mu_\nu - b^\mu b_\nu \right\} = 0. \quad (\text{A18})$$

This equation can be rewritten as

$$\begin{aligned} & \frac{1}{\alpha \sqrt{\gamma}} \partial_\mu \sqrt{\gamma} S_\nu V^\mu + \frac{1}{2\alpha} \frac{S_\alpha S_\beta}{S^t} \partial_\nu g^{\alpha\beta} \\ & + \partial_\nu \left(P + \frac{\|b\|^2}{2} \right) - \frac{1}{\alpha \sqrt{\gamma}} \partial_\mu \alpha \sqrt{\gamma} b^\mu b_\nu - \frac{1}{2} b_\alpha b_\beta \partial_\nu g^{\alpha\beta} = 0. \end{aligned} \quad (\text{A19})$$

To obtain the final form of the equations, multiply (A19) by the lapse α , split the μ index into its space (i) and time (t) components, and restrict ν to the spatial indices (j) only:

$$\begin{aligned} & \partial_t (S_j - \alpha b_j b^t) + \frac{1}{\sqrt{\gamma}} \partial_i \sqrt{\gamma} (S_j V^i - \alpha b_j b^i) \\ & = -\frac{1}{2} \left(\frac{S_\epsilon S_\mu}{S^t} + \alpha b_\mu b_\epsilon \right) \partial_j g^{\mu\epsilon} - \alpha \partial_j \left(P + \frac{\|b\|^2}{2} \right). \end{aligned} \quad (\text{A20})$$

The ν index can be restricted to the spatial indices because the equation that arises from $\nu = t$ for the time components of momentum and magnetic fields is redundant, corresponding to the total energy conservation equation. In our formalism, we solve the Eq. (A17) separately for the internal energy. Taking the following metric,

$$g_{\mu\nu} = \begin{pmatrix} -1 & 0 \\ 0 & \gamma_{ij} \end{pmatrix}. \quad (\text{A21})$$

where γ_{ij} is the spatial metric whose concrete description depends on coordinate system. Finally we describe our treatment of the gravity. Under the weak field limit, time-time component of the metric, g_{tt} , takes the form of $-(1 - 2\Phi)$ where Φ is Newtonian gravitational

potential (e.g. Shapiro & Teukolsky 1983). The third term of the momentum equation then becomes,

$$-\frac{1}{2} \frac{S^\alpha S^\beta}{S^t} \partial_j g_{\alpha\beta} \approx \rho h W^2 \partial_j \Phi. \quad (\text{A22})$$

Under this limit, Einstein equation becomes the Poisson equation for the gravitational potential (see Eq. (6)). Since the origin of the source term is the tt component of the energy momentum tensor, we replace ρ in the ordinary Newtonian limit with T_{tt} .

A.1. Energy Descriptions

We need to modify the description of energy from the Newtonian one to the special relativistic one. The total local energy, e_{local} , is defined by sum of the various energy:

$$e_{\text{local}} = e_{\text{kin}} + e_{\text{int}} + e_{\text{mag}} + e_{\text{grav}} \quad (\text{A23})$$

where e_{kin} , e_{int} , e_{grav} and e_{mag} is kinetic energy, internal energy, gravitational energy and magnetic energy, respectively. Their specific description is as follows:

$$e_{\text{kin}} = \rho W (W - 1), \quad (\text{A24})$$

$$e_{\text{int}} = e W^2 + p (W^2 - 1), \quad (\text{A25})$$

$$e_{\text{grav}} = -\rho h W^2 \Phi, \quad (\text{A26})$$

$$e_{\text{mag}} = \mathbf{B}^2 \left(1 - \frac{1}{2W^2} \right) - \frac{b^{02}}{2W^2}. \quad (\text{A27})$$

These descriptions are used for the calculations of the explosion energy in Subsection 5.4.

B. Special Relativistic MOC

The method of characteristics (MOC) is popularly used in the magneto-hydrodynamical simulations. In this algorithm the magnetic fields are evolved along the characteristic lines of the Alfvén waves. Detailed procedure for this algorithm for the Newtonian case is given in Stone & Norman (1992). For the special relativistic (SR) computations, we derive the solutions of the SR Alfvén waves in an analytic form,

$$\left. \frac{DW v_i + b_i / \sqrt{\rho h}}{Dt} \right|_- = 0, \quad (\text{B1})$$

$$\left. \frac{DWv_i - b_i/\sqrt{\rho h}}{Dt} \right|_+ = 0, \quad (\text{B2})$$

$$\left. \frac{D}{Dt} \right|_- \stackrel{\text{def}}{=} \frac{\partial}{\partial t} + \frac{v_j - \frac{b_j}{\sqrt{\rho h W}}}{(1 - b^t/\sqrt{\rho h W})} \frac{\partial}{\partial x_j}, \quad (\text{B3})$$

$$\left. \frac{D}{Dt} \right|_+ \stackrel{\text{def}}{=} \frac{\partial}{\partial t} + \frac{v_j + \frac{b_j}{\sqrt{\rho h W}}}{(1 + b^t/\sqrt{\rho h W})} \frac{\partial}{\partial x_j}, \quad (\text{B4})$$

where W , ρ , and h is the Lorentz factor, density and enthalpy respectively. v_j and b_j is the perpendicular component of the velocity and the magnetic field to the x_i directions.

In the subroutine for solving SR MOC in the code, the velocity and the magnetic fields are updated at half-time step along the characteristics using the above equations. By giving the analytic forms, it is readily seen that the speed of the propagation is guaranteed to be below the speed of light even for the regions where the density becomes low and the magnetic fields become strong, which is quite important for keeping the stable numerical calculations in good accuracy.

Alfvén Wave Propagation The propagation of a liner Alfvén wave is a basic test problem of MHD simulation. We consider a constant background magnetic field, B_x , and fluid velocity, v_x . And we add small transverse perturbations with velocity, v_z (v_y), and magnetic field, B_z (B_y). In this situation $b^t = \sum v^k b_k \approx v_j b_j$, therefore the analytic solution for the Alfvén wave becomes

$$\left. \frac{DWv_z + b_z/\sqrt{\rho h}}{Dt} \right|_- = 0, \quad (\text{B5})$$

$$\left. \frac{DWv_z - b_z/\sqrt{\rho h}}{Dt} \right|_+ = 0, \quad (\text{B6})$$

$$\left. \frac{D}{Dt} \right|_- \approx \frac{\partial}{\partial t} + \frac{v_x - \frac{b_x}{\sqrt{DhW}}}{1 - v_x \frac{b_x}{\sqrt{DhW}}} \frac{\partial}{\partial x}, \quad (\text{B7})$$

$$\left. \frac{D}{Dt} \right|_+ \approx \frac{\partial}{\partial t} + \frac{v_x + \frac{b_x}{\sqrt{DhW}}}{1 + v_x \frac{b_x}{\sqrt{DhW}}} \frac{\partial}{\partial x}. \quad (\text{B8})$$

If we take

$$Wv_z + b_z/\sqrt{\rho h} = 0, \quad (\text{B9})$$

the minus mode does not propagate. we assume $B_x = 0.09$, $v_x = 0.08$ for the Newtonian Alfvén wave and $B_x = 0.9$, $v_x = 0.8$ for the relativistic Alfvén wave. We take v_z as

$10^{-7}v_x \sin(2\pi x)$ and B_z is determined from b_z in Eq. (B9). The result is shown in Figure 12. In both Newtonian and relativistic cases, the form of the wave is not changed. It indicates that the computations are successfully performed in our code. The propagated waveforms are very smooth and no oscillations are found like the ones in the previous study (De Villiers et al. 2003).

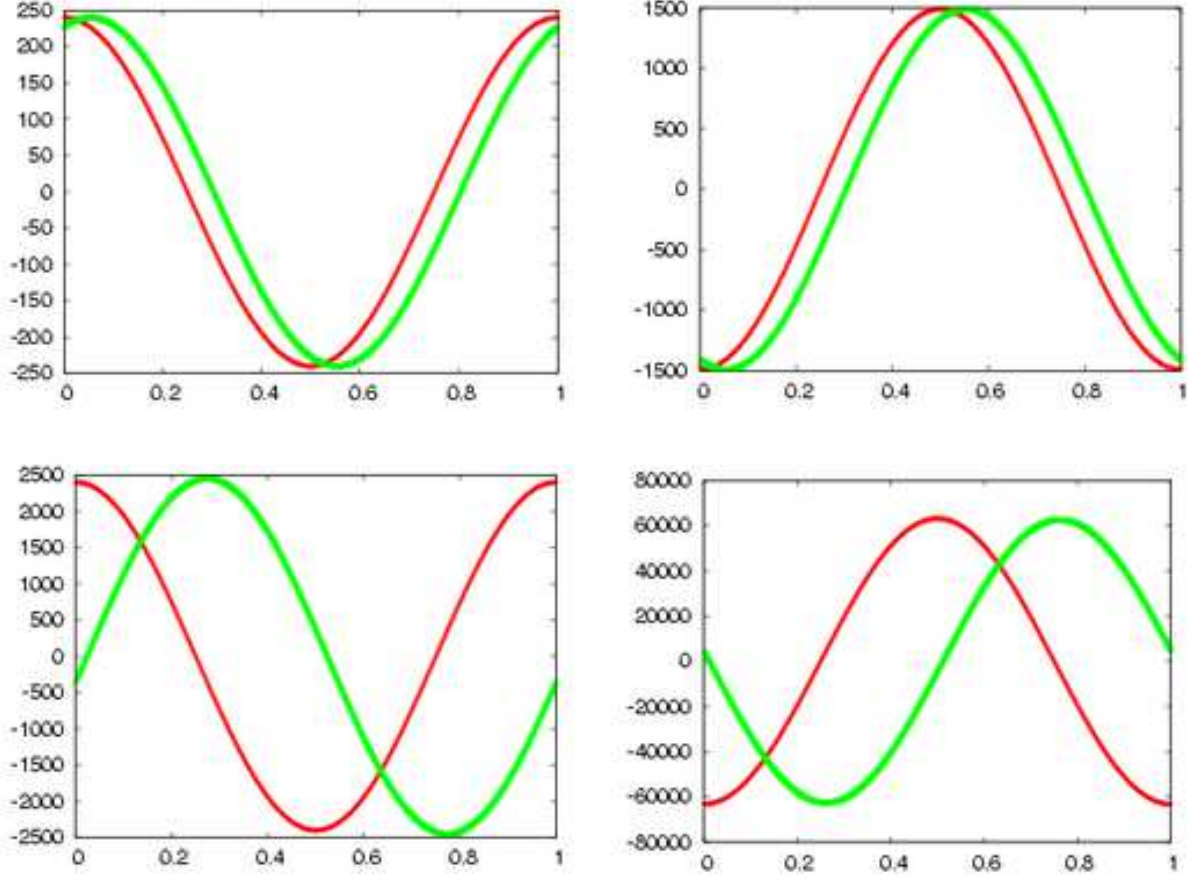


Fig. 12.— Top panels: Newtonian Alfvén wave propagation in z direction. The left figure show initial and final profile of v_z and the right one does that of B_z . Bottom panels: Relativistic Alfvén wave propagation in z direction. The left figure show initial and final profile of v_z and the right one does that of B_z .

C. Conservative Variable and Fundamental Variables

In our numerical code, variables such as hWv^i, D, E, B^i are evolved. These variables are called conservative variables. It is necessary to compute fundamental variables such as v^i, ρ, e, B^i from these conservative variables. In our computations, pressure is not described as an analytic function of energy e , therefore algorithms used in other GRMHD simulations (De Villiers et al. 2003) is not available here. If the value of the enthalpy, h , is found, the Lorentz factor, W , is obtained from the values of hWv^i and then all the fundamental variables are obtained. To determine the value of h , we search the root of the equation below:

$$f(h) \stackrel{\text{def}}{=} (1 + e/\rho + p/\rho + |b|^2/\rho) - h = 0 \quad (\text{C1})$$

where $|b|^2 = (B^2 + b_0^2)/W^2$. The fundamental variables in the equation is obtained when h is assumed, as stated above. We use simple bisection method to search the root of Eq. C1 and make the error of the equation, $\Delta h/h$, below 10^{-4} .

D. Test Problems

At last we show some results of the numerical tests on our code. We have done three typical problems in both non-relativistic case and relativistic case. Three problems are the shock tube problem, reflection shock problem and magnetic shock tube problem. We present the results one by one.

Shock Tubes We consider the shock tube used by Sod (Sod 1978) in his comparison of finite difference scheme. First we perform weak shock problem and strong shock problem in Newtonian case (Hawley et al. 1984b). For the weak one, the initial conditions of this problem gas with $\Gamma = 1.4$ with pressure and density $P_l = 1.0, \rho_l = 10^5$ to the left of $x = 0.5$ and $P_r = 0.1, \rho_r = 0.125 \times 10^5$ to the right. For the strong one, the initial conditions of this problem are gas with $\Gamma = 1.4$ with pressure and density $P_l = 0.67, \rho_l = 100$ to the left of $x = 0.5$ and $P_r = 0.67 \times 10^{-7}, \rho_r = 1.0$ to the right. The numerical value greatly correspond to the analytic value.

Next we perform relativistic shock tube problems. We fix the hydrodynamical variables except for the pressure of the left side, $\rho_l = 10, \rho_r = 1, p_r = 10^{-6}$ (Anninos et al. 2003). We set three types of pressure, i.e. $p_l = 1.33(W = 1.08)$ for lowly relativistic case, $p_l = 6.67(W = 1.28)$ for mildly relativistic case and $p_l = 666.7(W = 3.28)$ for highly relativistic case. The results are shown in the left panels of Figure 13. For lowly and mildly relativistic

case, the numerical value greatly correspond to the analytic value. For highly relativistic case, the velocity of the numerical comparison doesn't reach that of the analytic solution. It is due to the artificial viscosity which converted kinetic energy to internal energy.

Wall Reflections A second test presented here is the wall shock problem involving the shock heating of cold fluid hitting a wall at the left boundary. When the fluid hits the wall a shock forms and travels to the right, separating the pre-shocked state composed of the initial data and the post-shocked state with solution in the wall frame

$$V_S = \frac{\rho_1 W_1 V_1}{\rho_2 - \rho_1 W_1}, \quad (\text{D1})$$

$$P_2 = \rho_2 (\Gamma - 1) (W_1 - 1), \quad (\text{D2})$$

$$\rho_2 = \rho_1 \left[\frac{\Gamma + 1}{\Gamma - 1} + \frac{\Gamma}{\Gamma - 1} (W_1 - 1) \right], \quad (\text{D3})$$

where V_S is the velocity of the shock front, and the pre-shocked energy and post-shocked velocity were both assumed negligible ($e = V_2 = 0$).

The initial data are set up to be uniform across the grid with adiabatic index $\Gamma = 4/3$, pre-shocked density $\rho_1 = 1$, and pre-shocked pressure $P_1 = 10^{-6}$. And we change the velocity of the unshocked region parametrically. The result is shown in the right panels of Figure 13. For all computations, the differences between the numerical solution and the analytic one are small, however in case of relativistic one, pressure of the numerical solution is bigger than the analytic one. It is also due to the artificial viscosity assumed here.

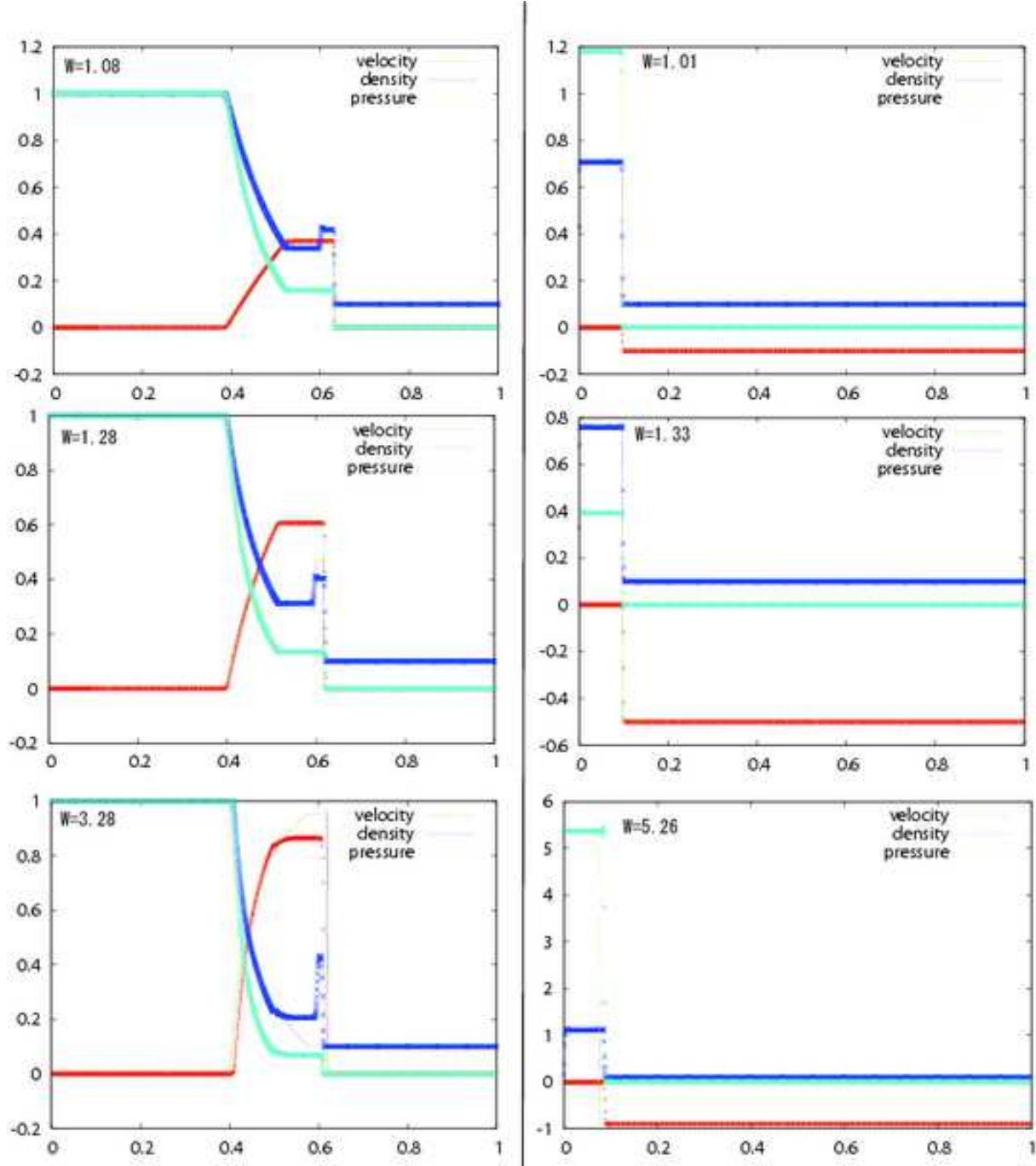


Fig. 13.— Left and right panel shows the shock tube and the wall reflection tests, respectively. From top to bottom, the Lorentz factor becomes larger (for right panels, top: $v = 0.1c$ ($W = 1.01$), middle: $v = 0.5c$ ($W = 1.33$), and bottom: $v = 0.9c$ ($W = 5.26$)). Note that the pressure and density is normalized by 100.

Magnetic Shock Tubes At last we present magnetic shock tube problems (Brio & Wu 1988). We show the initial condition and the results of the computations in Table 4. And we present mildly relativistic case in Figure 14, showing that our code can handle the various magneto-sonic waves as good as the code by De Villiers et al. (2003).

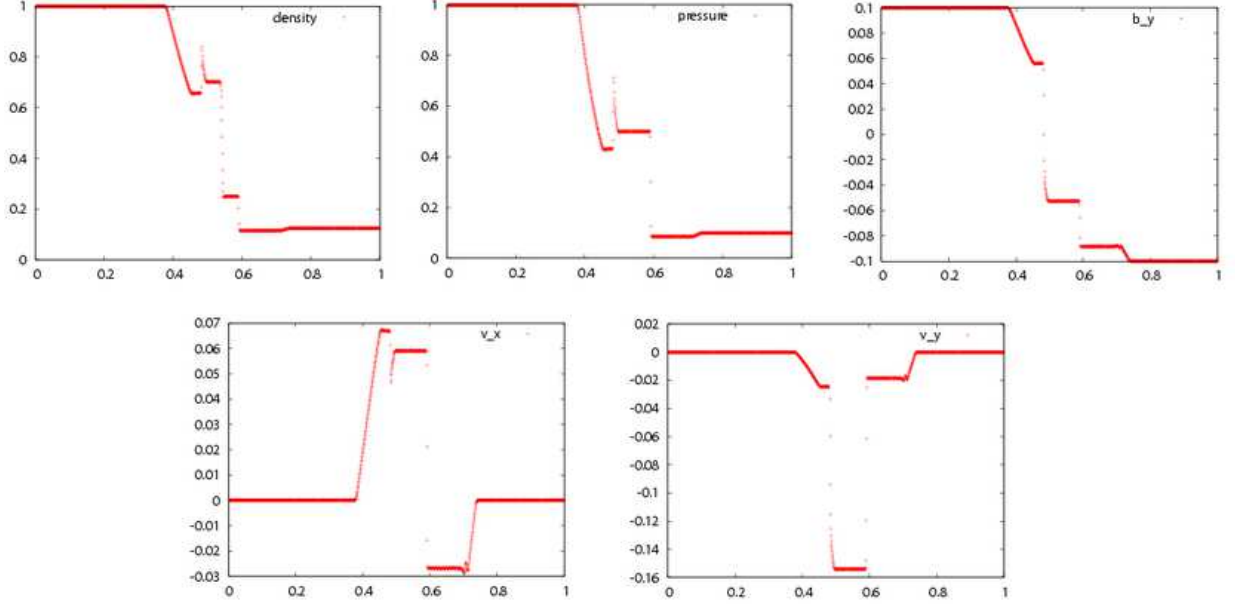


Fig. 14.— Mildly relativistic magnetic shock tubes

Table 4: Initial and intermediate states for shock tube tests. This table list the measured values in each state of shock tube: “Left” is the initial left state for the given variables, “FR” is the value of the variable at the foot of leftmost fast rarefaction fan, “SC” is the value of the peak of the slow compound wave, “CD_l” is the value of left of the constant discontinuity, “CD_r” is the value of right of the constant discontinuity, “FR” is the value of the variable at the foot of the second fast rarefaction fan and “Right” is the initial right state for the given variables,

Test	Variable	Left	FR	SC	CD _l	CD _r	FR	Right
Newtonian $B^x(\times 10^{-2})$ $= 0.75$	ρ	1.00	0.66	0.84	0.70	0.25	0.12	0.13
	$P(\times 10^{-4})$	1.00	0.44	0.73	0.50	0.50	0.09	0.10
	$v^x(\times 10^{-3})$	0.00	6.67	4.6	5.99	6.02	-2.79	0.00
	$v^y(\times 10^{-2})$	0.00	-0.25	-1.10	-1.58	-1.58	-0.20	0.00
	$\frac{B^y}{\sqrt{4\pi}}(\times 10^{-2})$	1.00	0.6	-0.5	-0.03	-0.54	-0.9	-1.00
Mildly	ρ	1.00	0.65	0.84	0.70	0.24	0.11	0.13
Relativistic $B^x(\times 10^{-1})$ $= 0.75$	$P(\times 10^{-2})$	1.00	0.42	0.71	0.49	0.49	0.08	0.10
	$v^x(\times 10^{-1})$	0.00	0.67	0.46	0.58	0.58	-0.26	0.00
	$v^y(\times 10^{-1})$	0.00	-0.24	-0.94	-1.5	-1.5	-1.9	0.00
	$\frac{B^y}{\sqrt{4\pi}}(\times 10^{-1})$	1.00	0.56	0.3	-0.52	-0.52	-0.88	-1.00
Relativistic B^x $= 0.75$	ρ	1.00	0.59	0.70	0.65	0.31	0.11	0.13
	P	1.00	0.51	0.60	0.47	0.47	0.08	0.10
	v^x	0.00	0.41	0.27	0.28	0.28	-0.12	0.00
	v^y	0.00	-0.07	-0.62	-0.58	-0.11	-0.11	0.00
	$\frac{B^y}{\sqrt{4\pi}}$	1.00	0.61	0.19	-0.24	-0.24	-0.81	-1.00